



Detector development at the Back-n white neutron source

Fan Ruirui^{1,2,3} · Li Qiang^{1,2,3} · Bao Jie⁴ · Li Yang^{1,2} · Liu Rong⁵ · Jiang Wei^{1,2} · Ren Jie⁴ · Zhang Qiwei⁴ · Cao Ping^{6,7} · Gu Minhao^{1,3} · Ren Zhizhou⁵ · Yi Han^{1,2} · Tang Jingyu^{1,2,3} · An Qi^{6,7} · Bai Haofan⁸ · Bai Jiangbo⁵ · Chen Qiping⁵ · Chen Yonghao^{1,2} · Chen Zhen^{6,7} · Cui Zengqi⁸ · Fan Anchuan⁹ · Feng Changqing^{6,7} · Feng Fanzhen⁹ · Gao Keqing^{1,2} · Han Changcai¹⁰ · Han Zijie⁵ · He Guozhu⁴ · He Yongcheng^{1,2} · Hong Yang^{1,2,11} · Hu Yiwei⁸ · Huang Hanxiong⁴ · Jia Weihua^{1,2} · Jiang Haoyu⁸ · Jiang Zhijie^{6,7} · Jin Zhengyao⁹ · Kang Ling^{1,2} · Li Bo^{1,2} · Li Chao^{6,7} · Li Gong⁹ · Li Jiawen^{6,7} · Li Xiao^{1,2} · Liu Jie⁸ · Liu Shubin^{6,7} · Luan Guangyuan⁴ · Ning Changjun^{1,2} · Qi Binbin^{6,7} · Ruan Xichao⁴ · Song Zhaohui¹⁰ · Sun Kang^{1,2,11} · Tan Zhixin^{1,2} · Tang Shengda^{1,2} · Wang Pengcheng^{1,2} · Wang Zhaohui⁴ · Wen Zhongwei⁵ · Wu Xiaoguang⁴ · Wu Xuan^{1,2} · Xie Likun^{6,7} · Yang Yiwei⁵ · Yu Yongji^{1,2} · Zhang Guohui⁸ · Zhang Linhao^{1,2,11} · Zhang Mohan^{1,3} · Zhang Xianpeng¹⁰ · Zhang Yuliang^{1,2} · Zhang Yue^{1,2} · Zhang Zhiyong^{6,7} · Zhao Maoyuan^{6,7} · Zhou Luping^{1,2,11} · Zhou Zhihao^{1,2,11} · Zhu Kejun^{1,3,11} · The CSNS Back-n Collaboration

Received: 31 October 2022 / Revised: 13 December 2022 / Accepted: 25 December 2022 / Published online: 13 January 2023
© The Author(s) 2023

Abstract

Purpose Back-n is a white neutron beamline at China spallation neutron source, which was established in the year of 2018. It is a powerful facility for nuclear data measurement, neutron detector calibration, and radiation effect research.

Method A series of detectors were built for different experiments, including beam monitoring, beam profile measurement, neutron induced secondaries (fission fragments, light charged particles and gamma) cross section measurement, and neutron resonance radiography, etc. A common digitization electronics and a cluster-based DAQ were developed for these detector systems. Most detectors have been employed at Back-n and serviced for experiments from the beginning of the beamline running.

Results and conclusion As an overview of detectors of Back-n, the details of the detector design and the experiment performing are described in this paper. Some developing systems, e.g., MTPC and B-MCP, are also included.

Keywords White neutron source · Beam diagnostics · Fission fragment · Charged particle · Gamma · Neutron resonance radiography

✉ Fan Ruirui
fanrr@ihep.ac.cn

¹ Institute of High Energy Physics, CAS, Beijing 100049, People's Republic of China

² Spallation Neutron Source Science Center, Dongguan 523803, People's Republic of China

³ State Key Laboratory of Particle Detection and Electronics, Beijing 100049, People's Republic of China

⁴ Key Laboratory of Nuclear Data, China Institute of Atomic Energy, Beijing 102413, People's Republic of China

⁵ Institute of Nuclear Physics and Chemistry, China Academy of Engineering Physics, Mianyang 621900, People's Republic of China

⁶ Department of Modern Physics, University of Science and Technology of China, Hefei 230026,

People's Republic of China

⁷ State Key Laboratory of Particle Detection and Electronics, Hefei 230026, People's Republic of China

⁸ State Key Laboratory of Nuclear Physics and Technology, School of Physics, Peking University, Beijing 100871, People's Republic of China

⁹ USTC archaeometry lab, University of Science and Technology of China, Hefei 230026, People's Republic of China

¹⁰ Northwest Institute of Nuclear Technology, Xi'an 710024, People's Republic of China

¹¹ University of Chinese Academy of Sciences, Beijing 100049, People's Republic of China

Introduction

Back-n is a white neutron source associated with the CSNS high energy proton accelerator, which has been running since 2018. The main motivation of this facility is for the nuclear data measurement and neutron detector calibration. More than hundreds experiments have been accomplished since the beginning of the operation, including $^{235}\text{U}/^{238}\text{U}$ fission cross section measurement [1], neutron induced light charged particle emission cross section measurement of ^6Li and ^{10}B [2,3], and others. Some of the results were collected by the EXFOR (Experimental Nuclear Reaction Data) [4] and evaluated by consultants on Neutron Data Standards [5].

Figure 1 shows the layout of the Back-n beamline and detectors' locations. The 1.6 GeV proton beam hits the tungsten target with a 15° deflection. The back-streaming neutrons are leading to the Back-n tunnel, which has a long flight distance for the neutron time-of-flight method. Two end stations ES#1 and ES#2 are constructed for different nuclear data measurements. The ES#1 has a distance of about 55 m, and ES#2 is about 70 m from the target.

The beam diagnostics and several detector systems, for example the Fission chamber, the light charged particle detector array, the C_6D_6 scintillation detectors and the camera system were developed before the beamline established and serviced most of the experiments at Back-n. Several ambitious developments, for example, the multi-purpose time projection chamber (MTPC), the radiation resistant semiconductor detectors, the Gamma-ray total absorption facility (GTAF-II) and the neutron-sensitive micro-channel-plate detector (B-MCP) are in progress for future experiments. The layout of the Back-n beamline and the locations of the detectors can be found in Fig. 1.

This article follows the classification of detectors, which can be divided into beam diagnostic systems, detector

systems for different particles, and neutron resonance radiography systems. It also includes the electronics and DAQ systems used by these detectors.

Detectors for neutron beam characterization and monitoring

Beam diagnostics is basic component for the beamline construction and running. Back-n has built an online flux monitor (Li-Si detector), a neutron energy measurement detector (Fission chamber) and a beam profile detector (Micromegas).

Li-Si beam flux monitor

A ^6LiF -silicon detector array was developed for real-time neutron monitoring at the back-n white neutron beam. It is installed on the beamline and works simultaneously with the nuclear data measurements to provide neutron flux data for normalization of the experiments [6].

To minimize beamline interference and background, the monitor was designed as a structure with a ^6LiF neutron conversion layer and Si detector array separated. ^6LiF is deposited on a $10\ \mu\text{m}$ Al film with a thickness of $360\ \mu\text{g}/\text{cm}^2$ and placed on the beamline with an area of $\phi\ 80\ \text{mm}$ covering the maximum beam envelope. Eight identical Si detectors are placed symmetrically on the side of the ^6LiF layer and upstream of the beam to reduce scattered neutron background. The sensitive area center of the Si detectors is on the diagonal of the beamline and the layer center. The bottom edge of the Si detector is outside the beam envelope to avoid direct irradiation by the neutrons. The monitor is shown in Fig. 2. It is entirely installed in the middle of a vacuum tube with a length of 40 cm and flanged to the other vacuum tubes on the beamline. Two Li-Si monitors were mounted in ES#1 and ES#2, and the distance between the ^6LiF layer and

Fig. 1 The layout of the back-n beamline and the detectors' location

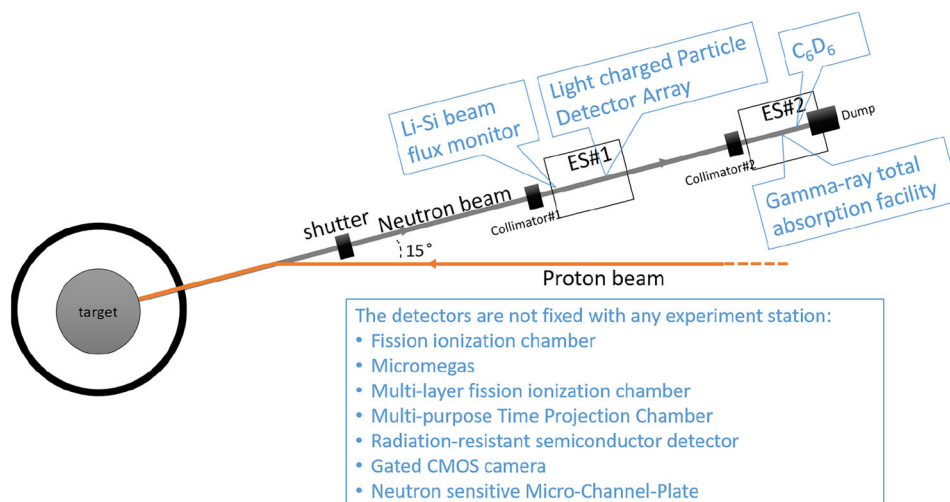




Fig. 2 Pictures of the Li-Si monitor

the tungsten target is 54.36 m and 73.76 m, respectively. A RF60 flange with nine vacuum-tight Lemo connectors is on the side of the tube. Electronic signals from the Si detectors are taken out through the connectors and connected to the input of MSI-8, a multi-function amplifier from Mesytec [7]. The voltage on the Si detector is -30 V and is supplied by a custom power supply, which was designed to supply voltages to both the Si and MSI-8 preamplifier.

The well-known cross section for the ${}^6\text{Li}(n, t){}^4\text{He}$ reaction allows to monitor the neutron flux from thermal to approximately 1 MeV energies [8]. The reaction products α and ${}^3\text{H}$ are emitted opposite to each other according to the principle of momentum conservation, which ensures that the Si detectors do not have double counting. The monitor count rate reflects the neutron fluence rate, which is consistent with the proton power on the target. The conversion factor requires a calibration using ${}^{235}\text{U}/{}^{238}\text{U}$ fission chamber, which gives measurement of the actual neutron fluence rate. Good performance was obtained when the Li-Si monitor was mounted on the beamline for monitoring experiments. Figure 3 shows the real-time online results obtained by the Li-Si monitor when CSNS operates at a frequency of 25 Hz and proton beam power of 100 kW. The (a) is a typical waveform of a neutron signal, and (b) is the integral spectrum of the signal pulse height, in which the peak of α -particles and tritons can be clearly identified. The (c) shows the online curve of count rate. Few downward spikes in the figure may be caused by the instantaneous drop of the beam power due to a flash fire or other reasons. Although the curve has a large fluctuation with the measuring time in figure (c), it has good stability after being normalized to the beam power. As shown

in (d), the counting rate is approximately 45.28 per 10 kW and the uncertainty is less than 1%, which includes statistical and systematic errors. The insert shows that there is a stable conversion factor between the proton flux and the monitor counts over a long period of time. In general, the calibrated monitor counts and integral protons can equivalently reflect the neutron flux during the monitoring period. In the case of stable energy spectrum of Back-n, the entire neutron flux can be obtained by a conversion factor and without having to detect neutron events over all the energy regions.

The cross section of ${}^6\text{Li}$ is very smooth and accurate in the neutron energy below 1 MeV. The detailed structure of the energy spectrum can be well measured by the monitor especially in the energy region below 10 keV, which are difficult to be analyzed by fission chamber with ${}^{235}\text{U}$ target, since the ${}^{235}\text{U}$ target has many resonances in the neutron cross section in this region [9]. The neutron energy is determined by the TOF method which defines the neutron velocity as $V = L/T$, where L is the flight path from the tungsten target to the ${}^6\text{LiF}$ layer and the T is the time-of-flight of neutrons obtained by the time interval between the time recorded by the detector and the trigger T_0 . For the neutrons below 10 keV, the effect of the ΔT is much less than 1%, and the ΔL can be calibrated by comparing the energy spectrum detail structure of the hyperthermal neutrons (1–10 eV) to that measured by the ${}^{235}\text{U}$ fission chamber. With determined L and T , the kinetic energy of neutrons can be calculated with the relativity formula. The neutron spectrum is obtained by dividing the counting rate by the cross sections of ${}^6\text{Li}$ extracted from ENDF-B/VIII.0 [10]. The result is normalized to 100 kW beam power and is shown together with the spectrum measured by the ${}^{235}\text{U}$ fission chamber with 100 bpd, as shown in Fig. 4 [11]. The energy spectrum below 10 keV measured by the monitor agrees with the spectrum measured by the ${}^{235}\text{U}$ target pretty well in the overall trend and without the resonance peaks. We compared the details of the two spectra in the energy region of 2.5–5 keV. As shown in the insert, the details of the two spectra outside of the resonance region can basically coincide.

Fission ionization chamber for neutron energy spectrum measurement

The fission chamber is dedicated to measuring neutron energy spectrum of Back-n, which is composed of several targets, electrodes, shielding, insulating parts, signal wires, inlet and outlet feedthroughs, etc., as shown in Fig. 5. The fission chamber adopts a copper shielding chamber and electrodes. The target substrate is a platinum plate with a thickness of 0.2 mm and a diameter of 32 mm. The diameter of the active area of the target is 20 mm. The total amount of the enriched uranium coating is 832.97 μg . The collection electrode, the target plate and the chamber are separated

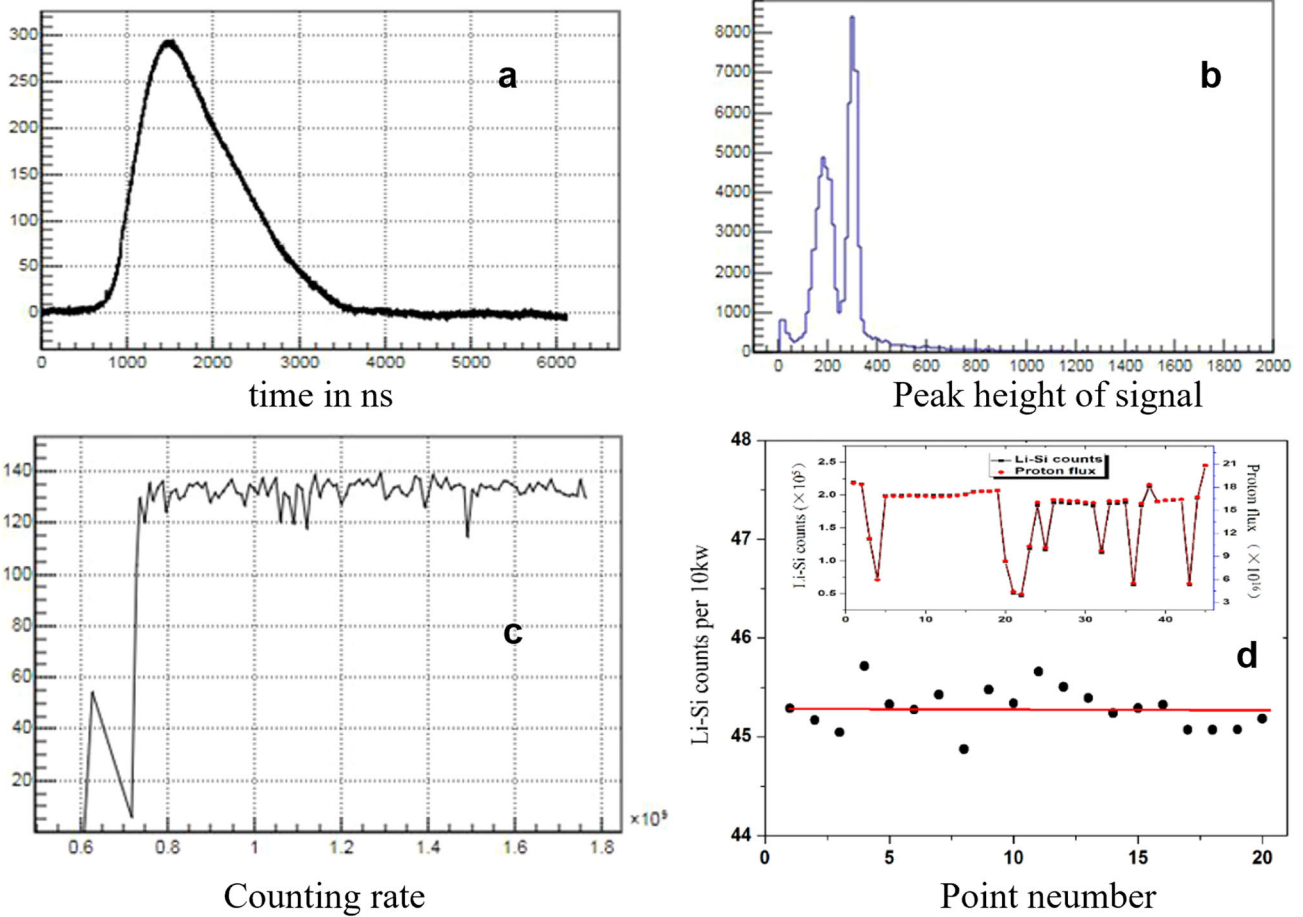


Fig. 3 **a** A typical waveform of a neutron signal; **b** the integral spectrum of the signal pulse height; **c** the online count rate curve of the monitor; **d** The monitor counts per second at 10 kW proton beam power. Comparison of the counts and proton flux in time stages is shown in insert [6]

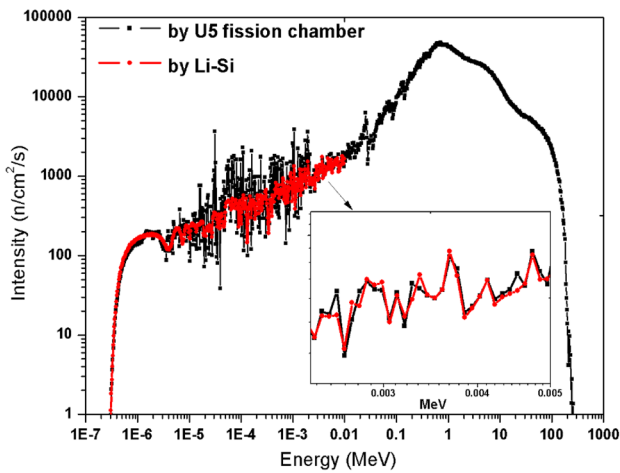


Fig. 4 The comparison of the neutron energy spectrum measured by the Li-Si monitor and the ^{235}U fission chamber. The detailed structure of 2.5–5 keV region is in the insert [6]

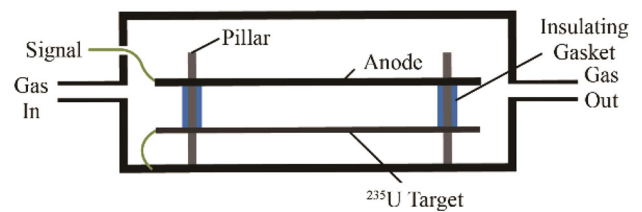


Fig. 5 Schematic diagram of the fission chamber for testing

ness of the insulating gasket. The target is grounded, and the collector is connected to the ORTEC-142B preamplifier, which is connected to a positive high voltage of 400 V. The fission chamber adopts a gas flow design, and the working gas is argon-methane P10 (10% methane, 90% argon).

The ability to distinguish noise and fission signals is obtained by adjusting parameters such as electrode spacing and voltage, in Fig. 6. The experimental results show that when the distance between the electrodes is small, the energy spectrum of the fission chamber is generally lower. The α decay events and fission events are mixed together; with the

by insulating materials, and the distance between the target plate and the collector is controlled by the varying thick-

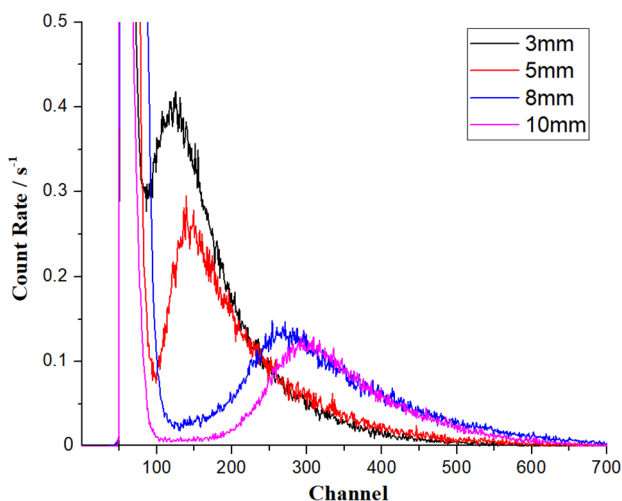


Fig. 6 Energy spectrum of ²³⁵U fission chamber with different plate spacing

increase in the distance between the plates, the fission fragment peak and the α peak are gradually distinguished, and the peak-to-valley ratio of the fission fragment is getting higher; when the distance reaches 10 mm, the identification between the fission fragment and the α particle can be counted more accurately.

Using the 14 MeV pulsed neutron beam generated by the D-T fusion reaction at the 600 kV Cockcroft-Walton generator of the China Institute of Atom Energy, the time correlation spectrum between the output signal of the fission chamber and the pick-up signal was measured, while the plate spacing was 10 mm, as shown in Fig. 7. The distance between the fission chamber and the tritium target head is 1.5 cm, and the neutron flight time is about 0.28 ns, which can be ignored. The rise time of the output signal of the fission chamber model was measured to be about 30 ns using an oscilloscope. With a Gaussian fitting, the FWHM of the fission signal peak is 30.97 channels in TAC, and the time resolution calculated according to the TAC channel width is 14.7 ns. The time resolution mainly comes from two contributions, the pulse width of the pulse beam and the time resolution of the detector. The pulse beam width is 2–3 ns, and the contribution to the time resolution is very small, so it can be considered that the measured time resolution is the detection time resolution of the device.

The fission reaction generally produces two fission fragments with opposite directions. When the direction is parallel to the target surface, both fragments cannot be detected. Therefore, the detection efficiency of the fission chamber is shown in Eq. 1, which is related to the number of target nuclei N , the fission cross section of $\sigma_f(E)$, and the detection efficiency ε_f of fission fragments, where ε_f is less than 100%. The neutron flux ϕ can be deduced by the companion particle method, and the detection efficiency of the fission chamber

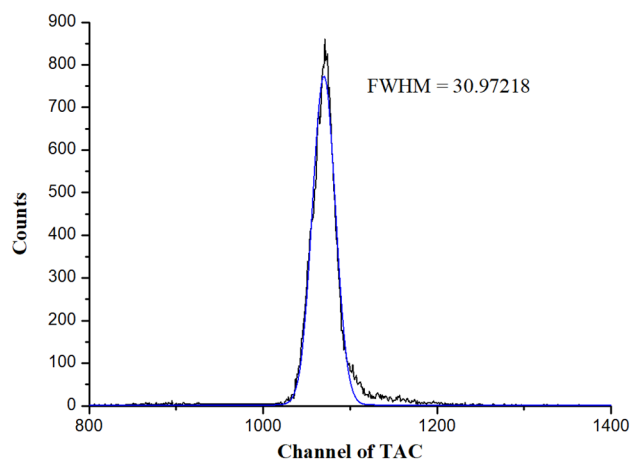


Fig. 7 Temporal correlation spectrum between the output signal of the ²³⁵U fission chamber and the pick-up signal

can also be obtained in combination with the fission chamber count rate N_f .

$$\varepsilon(E) = \frac{N_f}{\phi} = N \cdot \sigma_f(E) \cdot \varepsilon_f \tag{1}$$

As a result of calibration, with the 14 MeV neutron test, the detection efficiency is 4.3×10^{-6} , and the uncertainty is less than 5%. The final Back-n neutron energy spectrum measured by this calibrated fission chamber can be found in reference [11].

Micromegas for neutron beam profile measurement

Measurement of the neutron beam spot distribution is the basic requirement for the Back-n facility. Thanks to the good two-dimensional (2D) spatial resolution and fast timing capability of the Micromegas (micro-mesh gaseous structure) detector [12,13], it can be used for a quasi-online measurement of the neutron beam profile, e.g., at the n_TOF facility [14] and at the Back-n white neutron facility [15].

Micromegas detectors (MDs) have been widely used in nuclear and particle physics including rare event searches [16, 17] and neutron detection [18]. In this section, we present the development of an MD with 2D spatial resolution capability for the measurement of the neutron beam spot distribution. The current setup of the MD, used as a beam profiler at Back-n, sums up the neutron events of the entire energy range, with higher weights on low-energy neutrons due to higher cross sections $^{10}\text{B}(n, \alpha)^7\text{Li}$ and $^6\text{Li}(n, t)^4\text{He}$. However, it is planned, as part of the future detector development, to improve the MD system design so as to obtain the energy dependence of the neutron beam profile of Back-n.

Figure 8 shows the MD of this work. A thin layer of ^{10}B or ^6Li deposited on a thin aluminum foil is used as the neutron converter. The neutron converter is attached to the cathode

Fig. 8 Micromegas fabrication process. **a** The mesh after thermocompression bonding. An array of cylindrical pillars is visible, which hold the mesh and ensure a constant distance between the mesh and the PCB. **b** The detector chamber

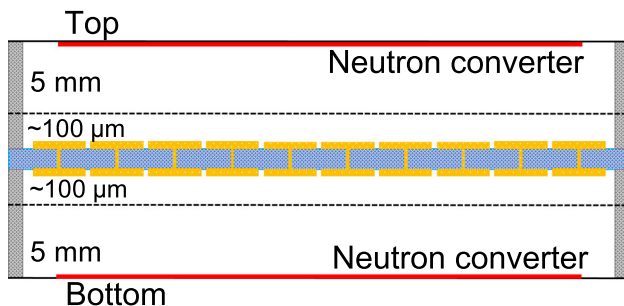
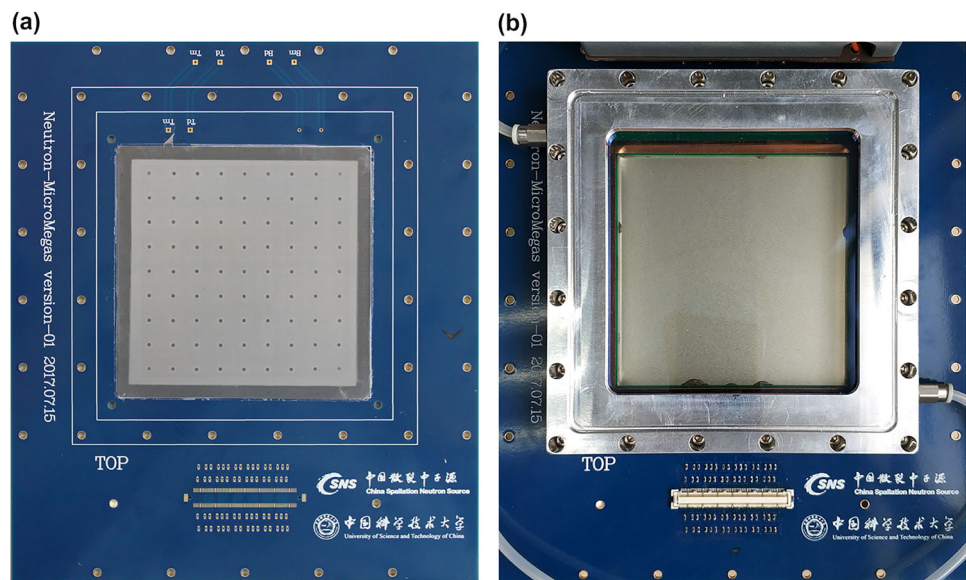


Fig. 9 Schematic of the MD with back-to-back double-avalanche structure. The mesh (dashed line) separates the 5 mm drift gap from the 100 μm avalanche gap. Each of the XY readout strips is independently connected to the central board

electrode facing the drift gap (i.e., the region between cathode and mesh). The mesh-anode avalanche gap (an amplification region where electron avalanches occur) is manufactured with the thermal bonding method (see Ref. [19] for detailed description of the manufacturing process). With this method, each side of the readout PCB is attached to a metallic mesh to form the avalanche gap, and a back-to-back structure are obtained (see Fig. 9). These two avalanche structures are able to work simultaneously for a higher detection efficiency. The avalanche gap and the drift gap are 100 μm and 5 mm, respectively. The total active area of the MD is 90 mm \times 90 mm. The layout and description of the MD are described in detail in Ref. [15].

Two detector units (namely MD-MA and MD-RA) with different anode designs are fabricated and characterized with a ^{55}Fe X-ray source to obtain the relative electron transparency, the gain and the gain uniformity, and the energy resolution [15]. For MD-MA, copper anode is used; for MD-

RA, resistive anode with germanium coating is used. The resistive layer protects the detector from discharges caused by possible intense ionization. Although the resistive anode MD-RA is relatively more complex to fabricate than the copper anode MD-MA, the former has higher gain than the latter. A dedicated front-end electronics system based on the AGET ASIC chip [20,21] is developed to process the anode strip signals [22]. In total, two AGET chips with 128 channels are used. The signal is amplified by a charge sensitive preamplifier and a shaping amplifier, and subsequently digitized by a multi-channel analyzer.

The neutron beam profile reconstruction capability of the detectors has been tested with an ^{241}Am α source, an Am-Be neutron source, and the CSNS Back-n neutron beam (Fig. 10). Figure 11 shows the 2D neutron beam profile at the Back-n ES#1 measured by the MD-MA with ^{10}B converter. The good agreement between the simulation and experimental data confirms the reliability of this measurement, as shown in Fig. 12 [15].

Detectors for measuring fission cross sections and light charged particle emissions

Back-n used a fast fission ionization chamber to measure fission fragments and an light charged particle detector array to measure light charged particles. In future experiments, fragmentation fragments and light charged particles tend to use the same kind of detector system. So a multi-purpose time projection chamber and next generation semiconductor detectors have been developed as an option.

Fig. 10 The MD together with the front-end electronics system was placed in the shielding container made of aluminum, as a neutron beam profiler at Back-n ES#1. The arrows represent the incoming neutron beam

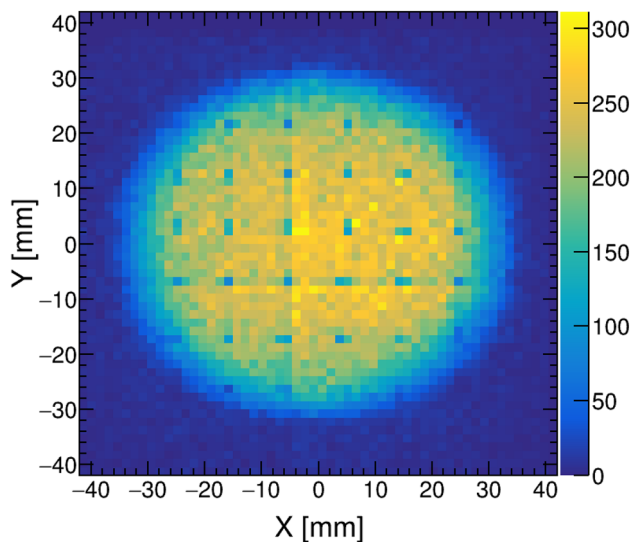
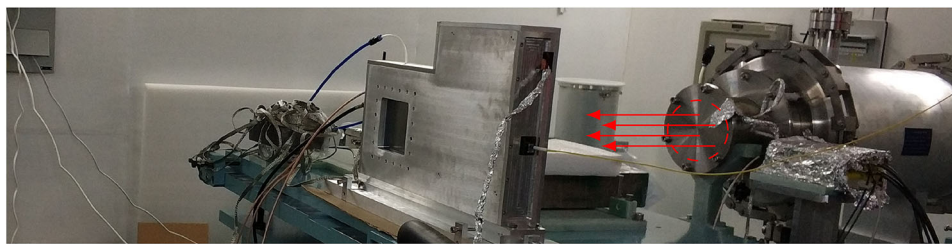


Fig. 11 The reconstructed 2D profile of the Back-n white neutron beam at ES#1. The bin widths for the 2D histogram are 1.5 mm on both the horizontal and vertical axes. The shaded dots in the profile image correspond to the reconstructed positions of the insulating pillars between the mesh and the anode plane

Multilayer fission ionization chamber

The fission ionization chamber as a reliable approach has been used for neutron induced fission cross section measurements for many years [23,24]. A multi-cell fast fission ionization chamber (FIC) has been developed as an initial detector for Fast Ionization Chamber Spectrometer for Fission Cross Section Measurement (FIXM) at Back-n [25,26]. FIXM contains FIC, front-end electronics, data acquisition (DAQ) system and peripheral supporting system and is mounted at the ES#2 as shown in Fig. 13.

FIC with an aluminum shell of $\phi 300 \text{ mm} \times 300 \text{ mm}$ and 5 mm thick is filled with a gas mixture of 90% Ar and 10% CF_4 at a pressure of 800 mbar. The two neutron beam windows of $\phi 80 \text{ mm}$ are sealed with 100- μm -thick Kapton films and located in the center of the fission chamber caps. There are eight independent cells including seven cells with high-purity fissile materials enriched over 99.94% and one blank cell inside the fission chamber and mounted along the direction of the neutron beam. Each cell consists of two electrodes of $\phi 80 \text{ mm}$ with a gap of 5 mm, in which the fission frag-

ments produced by fission reaction ionize the gas to generate signals. The gap, the capacitance and the high voltage of +200 V between electrodes are optimized in order to provide electrons having enough drift velocity, which is beneficial to obtain fast signals for high timing precision. A stainless steel of 20 μm thickness or aluminum foil of 100 μm thickness electroplated with the fissile material is the cathode, while the anode is made of aluminum foil of 100 μm thickness. The diameter of about 50 mm and uniformity of the fission coating are measured by the alpha-sensitive imaging method, and its mass is determined with the α -particle spectra measured in a small solid angle device [27]. The aluminum anode collects ionization signals by connecting to an 8-channel preamplifier MSI-8 in which the gain of each channel can be independently adjusted. The output signals of MSI-8 are entered in the common DAQ in which the signals are conditioned, digitized and stored. After several upgrades and performance tests at neutron sources, the improved FIC has a reliable and stable performance with the rise time of fission fragment signals of less than 30 ns from 10 to 90% and a high signal-to-noise ratio. The $^{236,238}\text{U}/^{235}\text{U}$ fission cross section ratios from threshold energy to tens MeV were measured by using FIC and time-of-flight method at Back-n, and the results verify the reliability of FIC [1,28]. FIXM could be used to measure fission cross sections of various isotopes covering a wide neutron energy region.

Light charged particle detector array

In cross section measurements of neutron induced light charged particles emission (n, lcp) reactions, detection and identification of charged particles are essential. Detection setups comprised of detectors, for example, grid ionization chambers, silicon detectors and scintillators, are usually adopted in previous measurements [29–33]. Based on these detection setups, particle identification (PID) of charged particles is realized with method such as ΔE - E method.

At Back-n, a light charged particle detection array (LPDA) has been built and applied to experiments. Sixteen units ΔE - ΔE - E telescopes are placed in a vacuum chamber with a diameter of 1 m. Each telescope is composed of a low-pressure multi-wire proportional chamber (LPMWPC) [34, 35], a 2.5 cm \times 2.5 cm PIN silicon detector and a cube CsI(Tl) detector with a side length of 3 cm. Thickness of each sil-

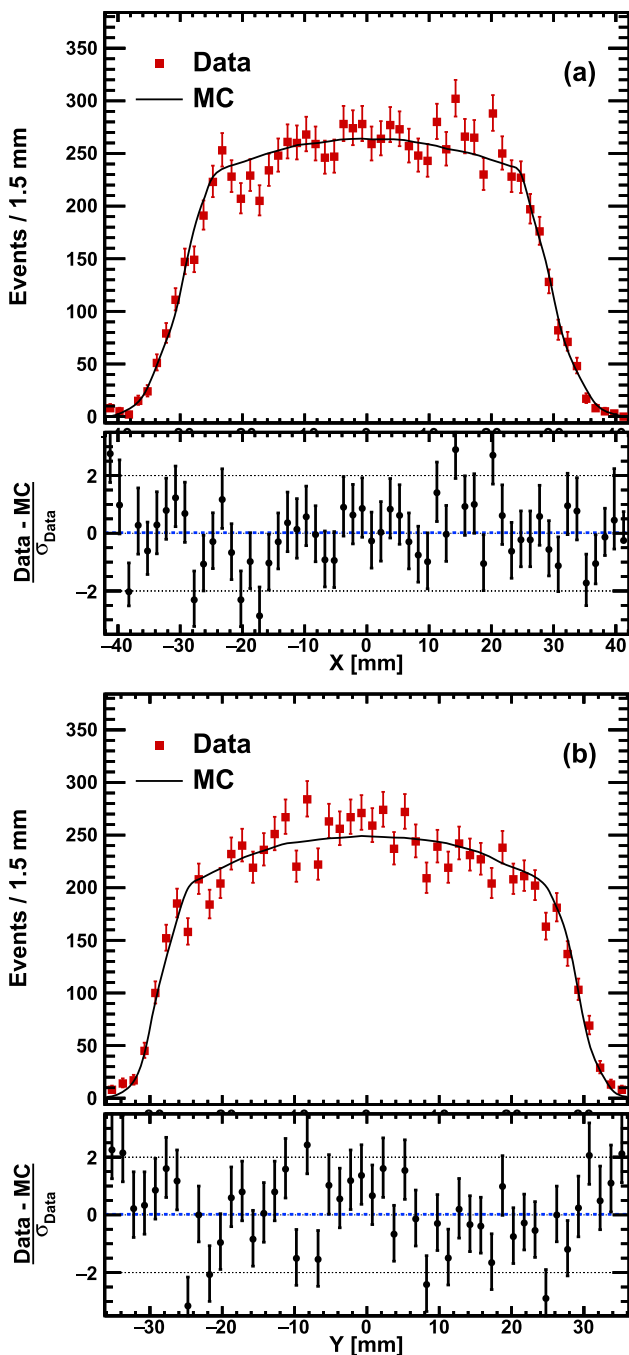


Fig. 12 The upper panels show the 1D projections of the slices of the 2D profile corresponding to **a** the middle Y-strip onto the X-axis and **b** the middle X-strip onto the Y-axis, for both data (solid squares) and MC simulation (solid curves). The expectation from MC simulation is normalized to data. The lower panels contain the significance of the deviation between the observed data and the simulation prediction in each bin of the distribution, considering only the statistical fluctuations in data



Fig. 13 Photograph of FIXM in Back-n beamline

icon detector is $300\ \mu\text{m}$. The angle between two adjacent telescopes is 9.5° . As Fig. 14 illustrates, with eight telescopes sealed in one cavity, the telescopes are divided into two identical parts. The entrance window of the cavity is replaceable, and a $4\ \mu\text{m}$ polypropylene foil is used as an entrance window in default. The distances between the surface of the LPMWPC, silicon detector and CsI(Tl) detector are 205, 214 and 222 mm, respectively. LPMWPCs and silicon detectors are connected to charge-sensitive preamplifiers that are mounted behind CsI(Tl) detectors in the cavity. Besides, optical signals produced in a CsI(Tl) detector are collected and converted to electric signal by a $2.1\ \text{cm} \times 2.1\ \text{cm}$ SiPM. During an experiment, the cavity will be filled with the working gas of the LPMWPC, usually 0.2 atm Ar+CO₂, which means that all detectors and charge sensitive preamplifiers in the cavity also work under the gas environment. To stable the pressure in the cavity, an air pressure control system is applied to ensure that the pressure in the cavity is $\pm 200\ \text{Pa}$ near the preset value. Besides, as Fig. 14 shows, a target holder on which four targets can be mounted is installed on the target chamber cover, and the center of different targets can be moved from top to bottom to the beam center position with the movement of the remote control motor.

In each telescope, the LPMWPC is used to identify the low-energy particles, and the CsI(Tl) detectors are applied to particles with higher energy. Results of an in-beam test indicate that using the $\Delta E-E$ method, protons in the energy range of 0.5 MeV to 100 MeV can be identified by the telescope [34]. Besides the $\Delta E-E$ method that two detectors required, the amplitude- E_n method and pulse shape discrimination method are also adopted to identified particles using silicon detectors [36]. In the amplitude- E_n method, E_n is deduced from the measured time-of-flight information. The amplitude- E_n method is utilized in $^{10}\text{B}(n, \gamma)^7\text{Li}$ and $^6\text{Li}(n, t)^4\text{He}$ cross section measurement reactions. Simulta-



Fig. 14 Photo of LPDA at Back-n. Sixteen telescopes are divided into two identical parts; the target holder is at the center of the vacuum chamber

neously, the pulse shape discrimination of silicon detectors is achieved with a charge and current sensitive preamplifier. The detector combination and PID method depend on the goal and emission particles' energy.

As part of the LPDA, a silicon detector array and $\Delta E-E$ telescopes have been applied to several experiments. Cross sections of $^{10}\text{B}(n,)^7\text{Li}$, $^6\text{Li}(n, t)^4\text{He}$, $^1\text{H}(n, n)^1\text{H}$ and $^2\text{H}(n, n)^2\text{H}$ reactions have been measured and published [3,37,38].

Multi-purpose time projection chamber

As a kind of detector with excellent three-dimensional tracking capability for measurements of particle momentum, spatial position, angular distribution and particle identification, time projection chambers (TPCs) have been widely used in particle and nuclear physics [39]. In recent years, TPC has also been adopted to the research of neutron nuclear data measurement [40], providing a new powerful tool for the cross sections of difficult measured with traditional methods.

To meet the requirements of nuclear data measurement, a multi-purpose time projection chamber (MTPC) is proposed at Back-n mainly for the light charged particle emission reaction, at the same time, other kinds of measurement such as fission reaction, neutron beam profile and neutron imaging can also be carried out with the MTPC.

A MTPC has been built and tested at Back-n. The schematic is shown in Fig. 15. The MTPC has a cylindrical sensitive volume of diameter of 140 mm. To form a uniform drift electric field, a height adjustable field cage shown in Fig. 16 composed of stacked PCB rings is designed to meet different measurements requirements. The readout anode PCB is connected at the end of the field cage. At the center of the anode PCB (Fig. 17), an array of 1519 hexagonal

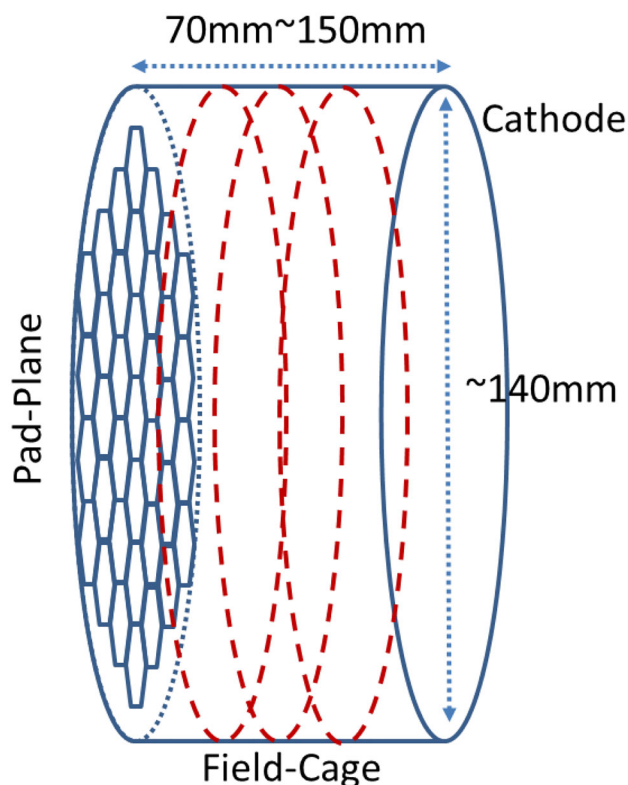


Fig. 15 The schematics of the MTPC structure

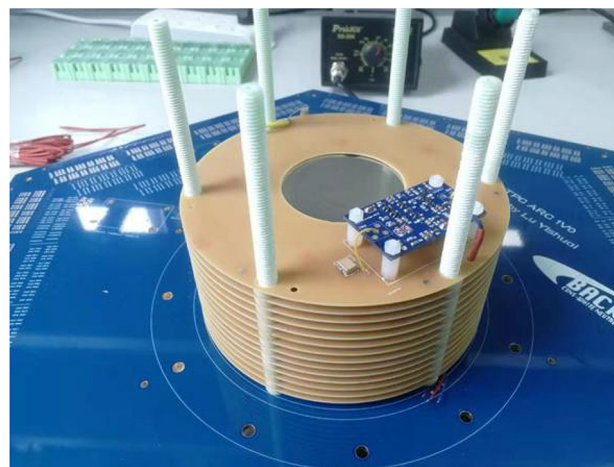


Fig. 16 The field cage of MTPC

pads is fabricated to collect the deposited charge. A resistive Micromegas structure [19] is stretched on the surface of the anode PCB for the purpose of ionization electron avalanche as shown in Fig. 18. With the coating of the high-resistance germanium film layer on the anode surface, the high-voltage stability of the detector is obviously improved and a higher spatial resolution is obtained due to the effect of charge dispersion on the resistive layer [41].

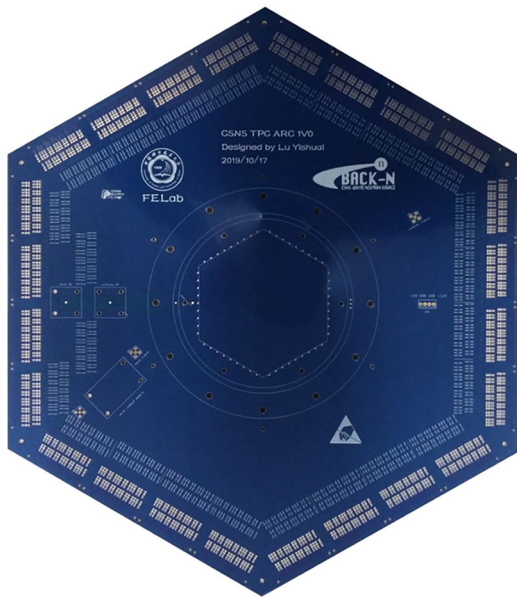


Fig. 17 The anode PCB of MTPC

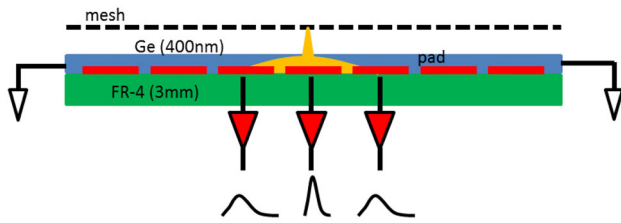


Fig. 18 The structure of micromegas

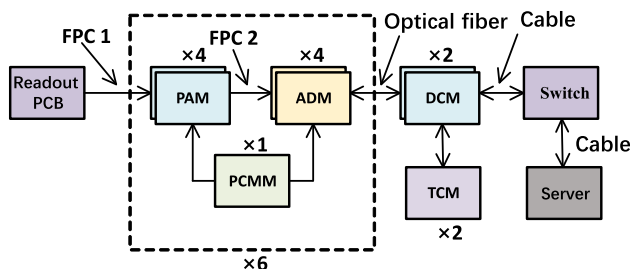


Fig. 19 The structure of electronics system

The structure of the electronics system of the MTPC is shown in Fig. 19. The introduction of the electronics system in details can be found in Ref. [42] and a brief introduction is given here. At the front-end of the system are the pre-amplifier module (PAM), the analog-to-digital module and the power clock management module (PCMM), and the back-end is composed of the data concentration module (DCM) and trigger clock module (TCM). The main parameters of the electronics system are listed in Table 1.

The MTPC has been commissioned with the white neutron beam at Back-n to verify its ability for measurements of neutron-induced reactions. In the beam test, a ^6Li sample is

Table 1 Key parameters of the electronics system

Sampling rate	40 MHz
Sampling window width	25.6 μs
Dead time	40 μs
Dynamic range	1.4 fC to 2.8 pC

mounted in the center of the cathode of the field cage. Figure 20 shows the typical track-display obtained in the beam test. For the track of triton, the Bragg distribution of dE/dx along the track is obviously identified, while the α -particle has a much shorter track because of larger mass and higher charge. The time-of-flight (TOF) distribution of all triggered events is shown in Fig. 21. The peak located at the small TOF region is caused by the high-energy neutron events, leading to a gap of dead time of about 40 μs . The distribution after the gap is mainly contributed from the reactions induced by neutrons on the ^6Li sample. A particle identification (PID) between triton and α -particle is shown in Fig. 22, verifying that the MTPC has a well PID ability which is limited if only the energy spectrum is obtained in the traditional method.

Currently, the finalized MTPC has been proposed and the new version of detector facility is under manufacturing. With this newly developed TPC detector system, a physical experiment will be conducted at the Back-n beamline in the nearly future.

Radiation-resistant semiconductor detector

Because of the excellent radiation resistance performance, wide-band gap semiconductor detectors are considered as an optimal option for silicon detectors. Among the wide-band gap semiconductor detectors, SiC and diamond detectors are widely studied for particle detection [43–46]. SiC and diamond detectors have the advantages of neutron and proton irradiation resistance, working normally at high temperatures [47–49]. In addition, due to the faster carrier drift speed and higher breakdown field strength, the rise time of output signals is faster than silicon detectors'. Thus, these detectors are suitable for fast measurement or time measurement [50].

4H-SiC detectors have been manufactured and tested at Back-n. The thickness of the substrate of the N-type 4H-SiC detector is 370 μm , and the N-type 4H-SiC epitaxial material is produced by Cree Company. The epitaxial layer includes an N+ type 4H-SiC buffer layer with a thickness of about 500 nm and a 21 μm -thick N-type 4H-SiC epitaxial layer with a doping concentration of $1.5 \times 10^{14} \text{ cm}^{-3}$. A Ni/Au Schottky contact electrode with an area of 1 cm^2 was fabricated on the epitaxial layer, and an Al/Ti/Au ohmic contact electrode with an area of 1 cm^2 was fabricated on the substrate side.

The single-crystals diamond used at Back-n is high-quality single diamond crystals prepared by Zhengzhou

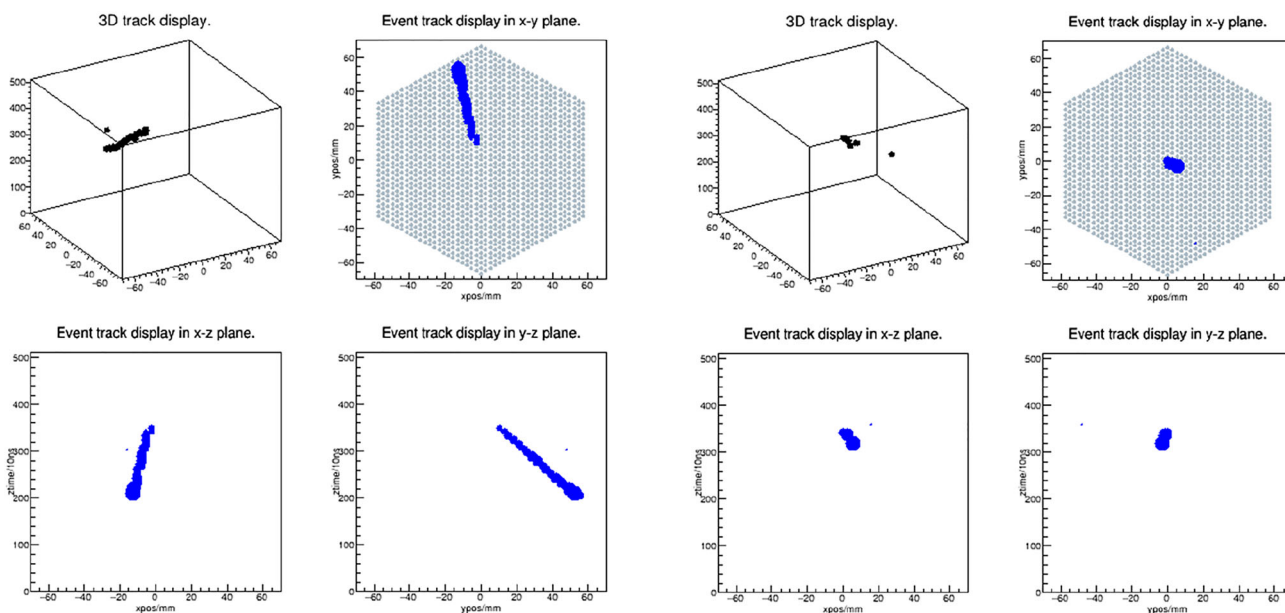


Fig. 20 Typical tracks of triton (left) and -particle

University by microwave plasma chemical vapor deposition (MPCVD) and commercial detector-grade single diamond crystals produced by Element Six Company, with a size of $5.6 \times 5.5 \times 0.64 \text{ mm}^3$ and $4.5 \times 4.5 \times 0.5 \text{ mm}^3$, respectively. After multi-step cleaning, titanium and gold circular electrodes were evaporated on both sides of the single diamond crystal using thermal evaporation technology to form ohmic contacts and prevent metal oxidation, separately. Annealing at $650 \text{ }^\circ\text{C}$ for 40 minutes ensures that a layer of Ti and C compounds is formed on the surface of the titanium and diamond, which increases the adhesion and reduces the potential barrier.

SiC and diamond detectors have been adopted to several cross section measurements and show good performance during experiments. Nevertheless, the area of diamond detectors and thickness of SiC detectors are still needed to be improved.

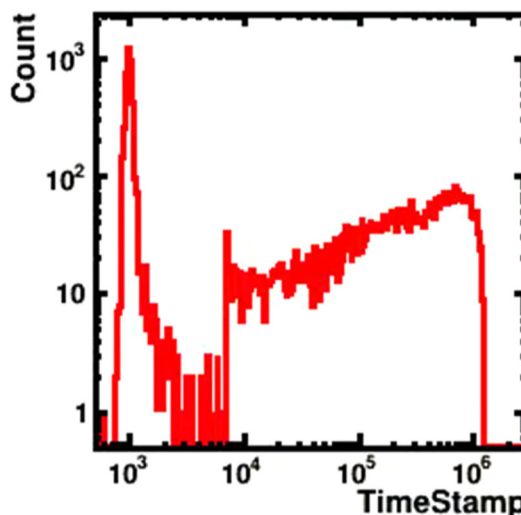


Fig. 21 TOF distribution

Detectors for measuring reaction gammas

Radiative neutron capture cross section ($\sigma_{n\gamma}$) is of primary importance in studies of stellar nucleosynthesis, designs of advanced nuclear reactors, and applications of nuclear technology. Nowadays, mainly three kinds of detectors for $\sigma_{n\gamma}$ measurement are used: total γ -ray absorption detectors, known as $4\pi \text{ BaF}_2$ detector array [51], total energy detection system, such as C_6D_6 [52], and high-resolution γ -ray detectors, such as HPGe detectors [53]. Since HPGe detectors are currently being designed and procured, only the first two are included in this section.

C_6D_6 detection system

A detection system with four C_6D_6 liquid scintillation detectors was chosen as the first $\sigma_{n\gamma}$ measuring equipment at Back-n for its low neutron sensitivity, fast time response, and simple structure [54]. This C_6D_6 detection system was installed at the center of ES#2 of Back-n, about 76 m away from the spallation target, shown in Fig. 23. The C_6D_6 liquid scintillator was 127 mm in diameter and 76.2 mm in length, contained in a 1.5-mm-thick aluminum capsule and coupled with a photomultiplier tube (PMT). These C_6D_6 detectors were placed upstream of the sample relative to the neutron

Fig. 22 PID of experimental data

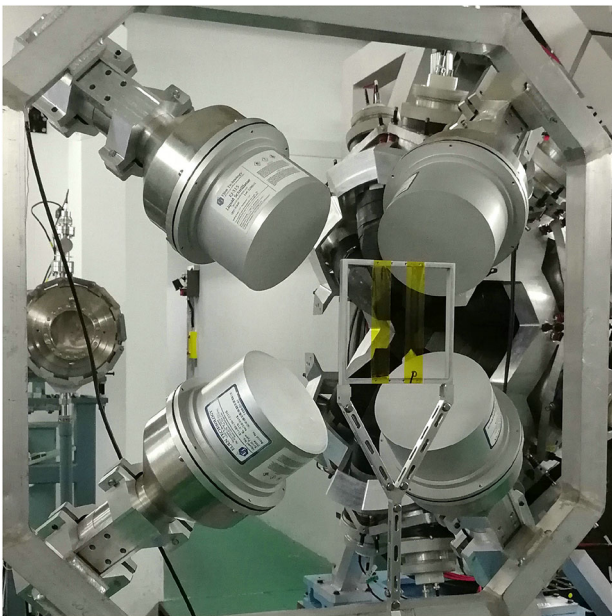
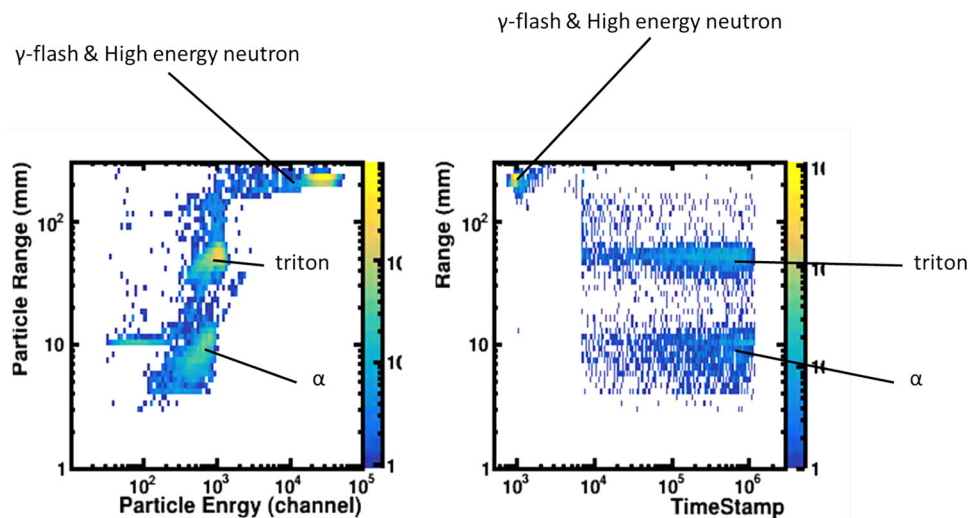


Fig. 23 Photograph of the C_6D_6 detection system at Back-n

beam, and the detector axis is at an angle of 125 degrees with respect to the neutron beam direction. The distance between the center of the front face of the detector and the sample center is about 150 mm. Anode signals delivered by the PMTs were recorded by the Back-n general-purpose Data Acquisition System (DAQ) [55], which digitizes the analog signals into full-waveform data with a sampling rate of 1 GS/s and a 12-bit resolution.

To obtain high precision $\sigma_{n,\gamma}$, the weighting function (WF) of the C_6D_6 detection system was calculated with the pulse height weighting technique (PHWT) [52,54] and the experimental backgrounds were determined with dedicated

measurements and Monte-Carlo simulations [56]. Besides, the resolution function was also studied to analyze the resonance parameters of ^{232}Th and other nuclides [57]. With these studies, the $\sigma_{n,\gamma}$ in the energy region between 1 eV and 400 keV can be measured with this C_6D_6 detection system [58,59].

Gamma-ray total absorption facility

Gamma-ray total absorption facility (GTAF-II, which is the upgraded version of the earlier GTAF [60] according to the experiment of Back-n) has been constructed for accurate $\sigma_{n,\gamma}$ measuring by prompt gamma method, which consisted of 40 barium fluoride detector units [61], shown in Fig. 24. The excited states in the compound nucleus that are populated by neutron capture can decay via many different gamma-ray cascades. The principle of detection is the sum energy of the cascade that corresponds to the binding energy of the captured neutron plus the kinetic energy of the captured neutron, it is usually about 6~8 MeV. The BaF_2 crystal shell with a thickness of 15 cm and an inner radius of 10 cm was subdivided into 12 pentagons and 28 hexagons, which covered 95.2% of the solid angle. The overall time resolution (FWHM) of GTAF-II was 23.7 ns, and the detection efficiency of ^{60}Co cascade gamma rays was 90% [62]. The $\sigma_{n,\gamma}$ experimental data of ^{197}Au [63] and ^{169}Tm were measured (neutron flight distance of 75.9 m). The position of resonance peak could be well consistent in comparison with the relevant data of ENDF evaluation database, which verified the reliability of GTAF-II and measurement technology. In the next step, high precision $\sigma_{n,\gamma}$ of fission nuclides and radioactive nuclides could be obtained by deducting the background and improving the effect background ratio.



Fig. 24 Photo of GTA-F-II at Back-n

Detection systems for neutron resonance radiography

Thanks to the highest flux of the white neutron beam in the world, Back-n may have the best opportunity for the neutron resonance photography. The principle can be found in reference [64]. Two different systems are been developing tested at Back-n. A CMOS camera is a traditional image system, while the neutron-sensitive micro-channel-plate is still a novel technique.

Gated CMOS camera

A detector system with CMOS camera is constructed at Back-n white neutron source, which is mainly used in beam spot measurement, scintillator calibration, neutron imaging and

other experiments. The system mainly consists of CMOS camera, neutron conversion scintillator and optical mirror, which are packaged in a light-shielding box, as shown in Fig. 25a.

The neutron conversion scintillator usually uses EJ426, which is still a novel technique for thermal neutrons with low sensitivity to gamma radiation [65]. The scintillator is a ZnS screen doped with ^6LiF , and the thermal neutron detection efficiency of 0.5 mm thick is about 34%. As shown in Fig. 25b, the screen is placed in the center of the neutron beam, and its plane is perpendicular to the beam direction to detect neutrons by the well-known cross section of $^6\text{Li} + \text{neutron} \rightarrow ^3\text{H} + ^4\text{He} + 4.78 \text{ MeV}$. The CMOS camera was purchased from Oxford Instrument Company, and its sensor size is $16.4 \times 14.0 \text{ mm}^2$ with 2560×2160 pixels. The typical spatial resolution of the camera is about $130 \mu\text{m}$. This camera has the ability to delay and select the time window, and the gate delay and width are adjustable from 0 to 10 s with the highest precision of 10 ps. The neutron energies are measured by the time-of-flight method. Therefore, this function of the camera can enable it to achieve energy-division photography and energy-resolved imaging on the Back-n.

Since March 2018, the camera system has carried out experiments such as standard beam spot measurement, scintillation screen calibration and neutron photography on the Back-n. A lot of research achievements have been obtained. As shown in Fig. 26, the $\phi 50 \text{ mm}$ mode neutron profile distribution and grayscale information on x and y axis measured in the ES #1 [66]. The beam spot distribution is independent of the neutron energy. For the neutrons with energy above 0.5 MeV, a more suitable plastic scintillator can be used instead of the ZnS(^6Li) screen. The standard beam spots in different modes of the Back-n are important beam parameters for the

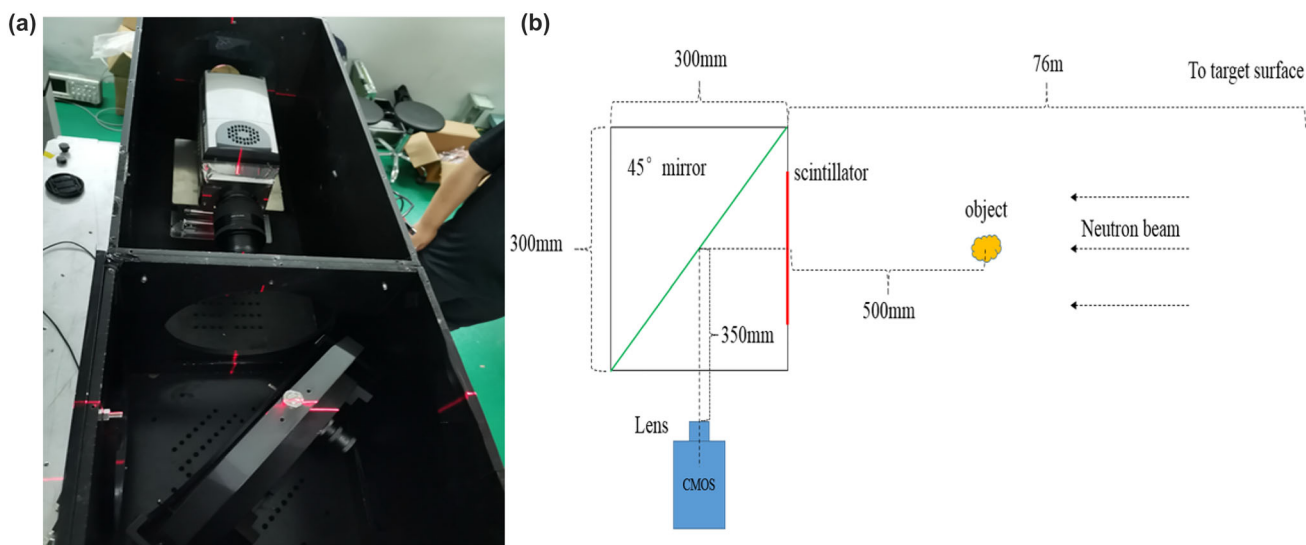


Fig. 25 a Photograph and b schematic view of the imaging detector system

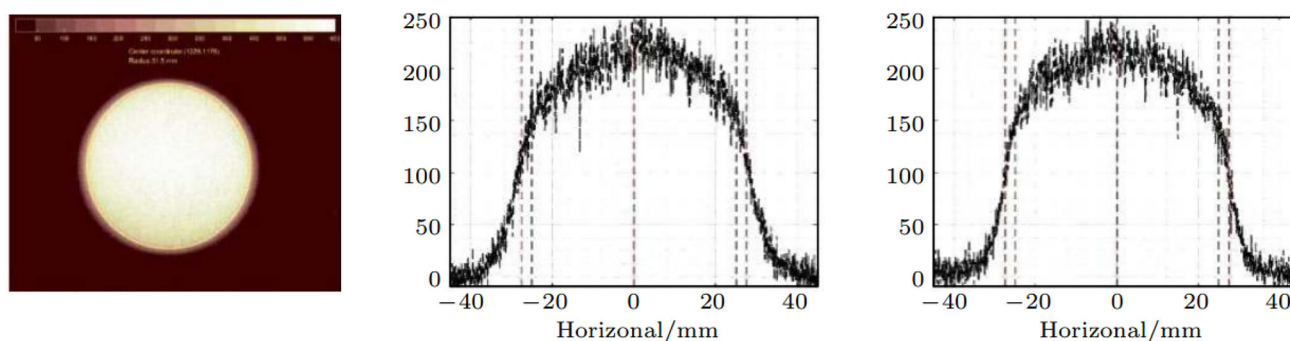
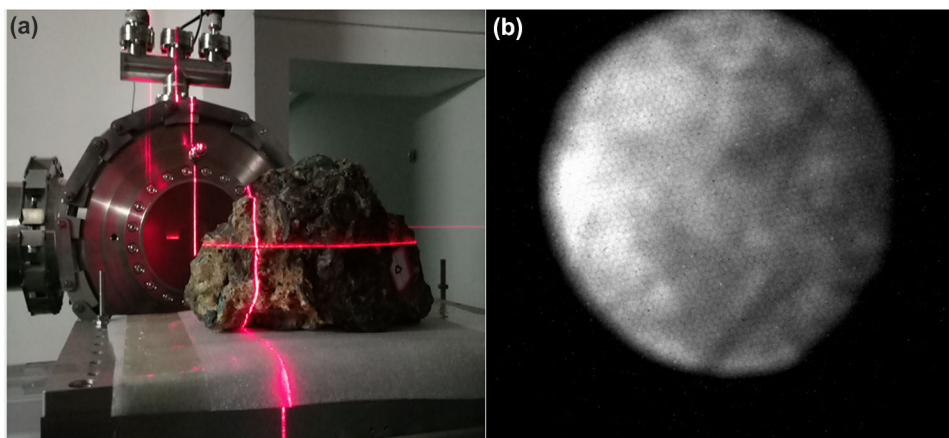


Fig. 26 Neutron profile distribution and grayscale information on x and y axis [1]

Fig. 27 **a** Photograph and **b** neutron imaging of internal structures of the irregular marine condensate



user experiments such as nuclear data measurement, radiation effect and neutron radiography.

For neutron radiography experiments, a remotely controlled FIXM sample platform is used to move a series of samples horizontally and vertically to save experimental time significantly. A rotating platform is used for neutron CT experiments. Neutron radiography is a method for investigating the inner structure of samples [67]. Compared with X-ray radiography, neutron radiography has a natural advantage in nuclide identification as neutron attenuation depends on the nuclear reaction between nucleus and neutron. Back-n has great potential in obtaining large-scale sample images due to its high flux and high-energy neutrons. Fig. 27a and b shows photograph and neutron imaging of internal structures of the irregular marine condensate, in which the shape of the ancient coins is clearly visible. The energy-selective photography of the CMOS camera enables it to perform nuclide resonance imaging measurements on the Back-n. In the resonance imaging, the neutrons with different energies are transmitted through the sample, then multiple radiographs are recorded by the camera with and without resonance neutrons. The nuclide components can be implied by processing the images [68]. Benefiting from the wide energy spectrum and high flux of the Back-n, various nuclides with cross section resonances in different energy regions are studied.

Neutron-sensitive micro-channel-plate

A neutron detector with energy and position resolution based on a ^{10}B -doped micro-channel plate (B-MCP) is being under development on the Back-n. The B-MCP has high temporal resolution, spatial resolution, and high neutron detection efficiency. With the advantages of wide energy spectrum and high flux of Back-n, it is very suitable for neutron resonance imaging experiments. The B-MCP detector is generally composed of neutron-sensitive B-MCP group, readout anodes, vacuum chamber and voltage sources. Its main structure is shown in Fig. 28.

The neutrons react with the sensitive nuclide ^{10}B in the B-MCP to produce secondary particles α and ^7Li , which excite secondary electrons on the inner wall of the B-MCP channel. The secondary electrons multiply in the channel under electric field to generate more secondary electrons and finally form an electron cloud at the exit of the channel to enhance the signal of the neutron event. To increase the collision probability between electrons and the channel and suppress ion feedback, the channel has an angle of about $5^\circ \sim 10^\circ$ relative to the MCP surface normal, and generally, two MCP are used in combination with a V-shape of their channels. The ^{10}B is one of the commonly neutron-sensitive nuclides, and its secondary particles α and ^7Li have a short range of only about

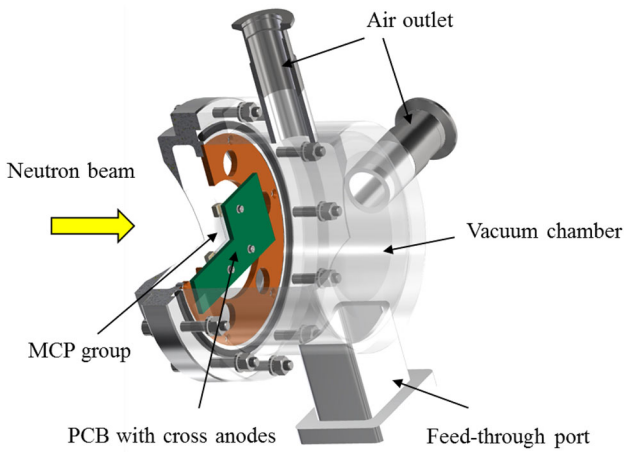


Fig. 28 Schematic diagram of the structure of the B-MCP detector

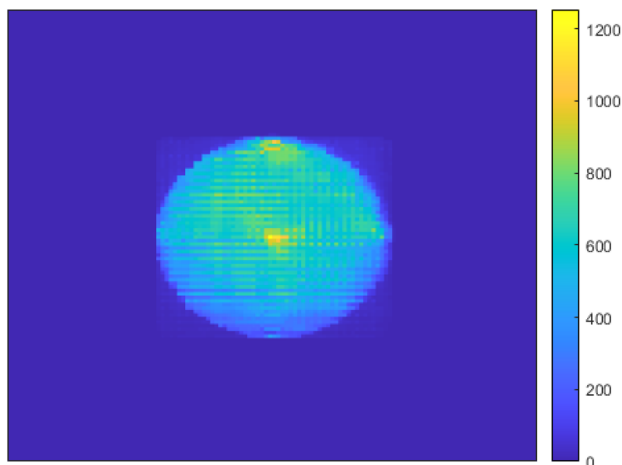


Fig. 29 The $\phi 30$ mm beam profile in the #ES2 measured by the B-MCP detector

$2 \sim 3.5 \mu\text{m}$. Therefore, the secondary electrons are basically multiplied in several adjacent channels, and the spatial resolution of MCP can be better than $10 \mu\text{m}$. The transit time of secondary electrons in the MCP channel is at the ps level. The B-MCP can accept very high count rate with excellent time resolution. The detector system count rate limit and time resolution depend primarily on the electronics. The readout anodes of the B-MCP use an array of anode strips for the high flux neutron sources. The analytical spatial resolution of the charge center of gravity method can reach several tens of microns, which is sufficient for fast neutron imaging in most cases. B-MCP normally works at a vacuum of about $10^{-4} \text{ Pa} \sim 10^{-5} \text{ Pa}$. Therefore, the detector system needs to be sealed in a vacuum chamber. The ^{10}B -doped B-MCP used in our experiments is about 10 mol% content of the ^{10}B nuclide. The test samples have a diameter of 33 mm and a thickness of 0.5 mm. We carried out beam spot measurements on Back-n using the B-MCP detector and studied the response of B-MCP to neutrons in different energy regions.

As shown in Fig. 29, the measured $\phi 30$ mm beam profile in the #ES2 is clearly displayed, indicating that the development of the B-MCP detector is basically in line with expectations. The simulation study on signal response of the B-MCP is also carried out to provide a reference for the experimental analysis. The domestic development of ^{10}B -doped B-MCP technology is being carried out in cooperating with the North Night Vision Technology Research Institute Co.Ltd, and it is difficult to dope ^{10}B with high concentration consistence. Therefore, it is of great significance to study the properties of ^{10}B -doped B-MCPs on Back-n.

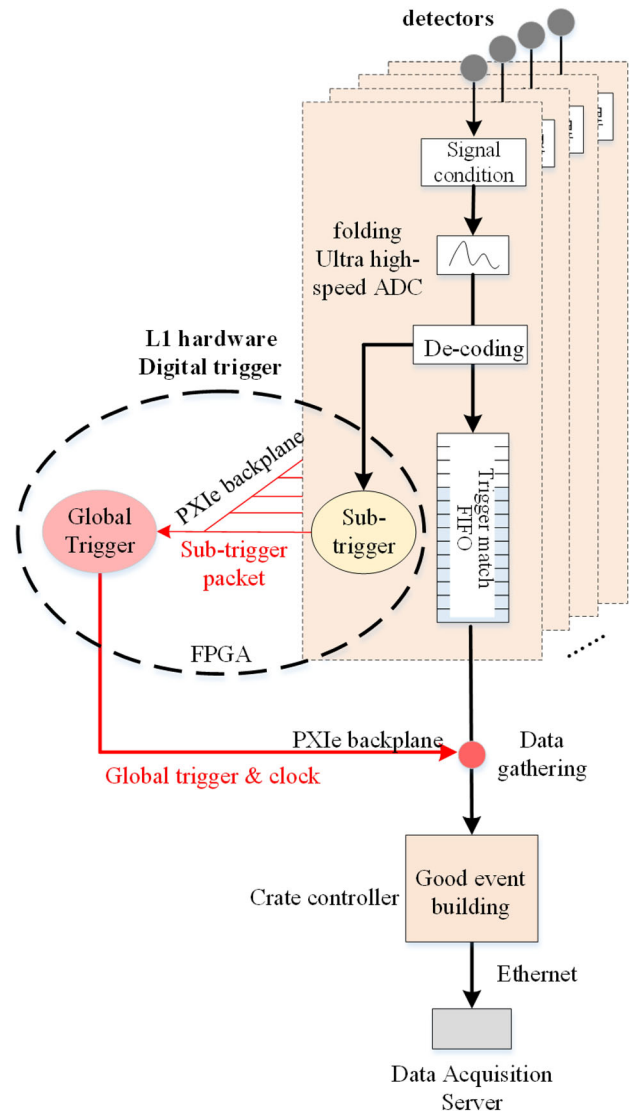


Fig. 30 Structure of full digital trigger mechanism

Fig. 31 Structure of readout electronics

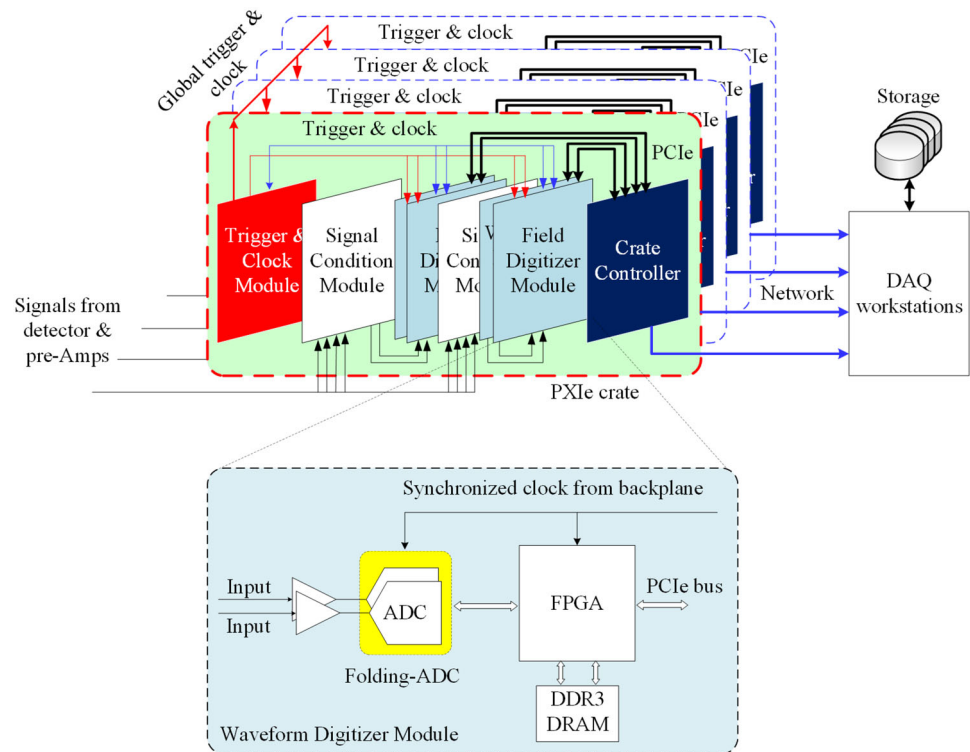


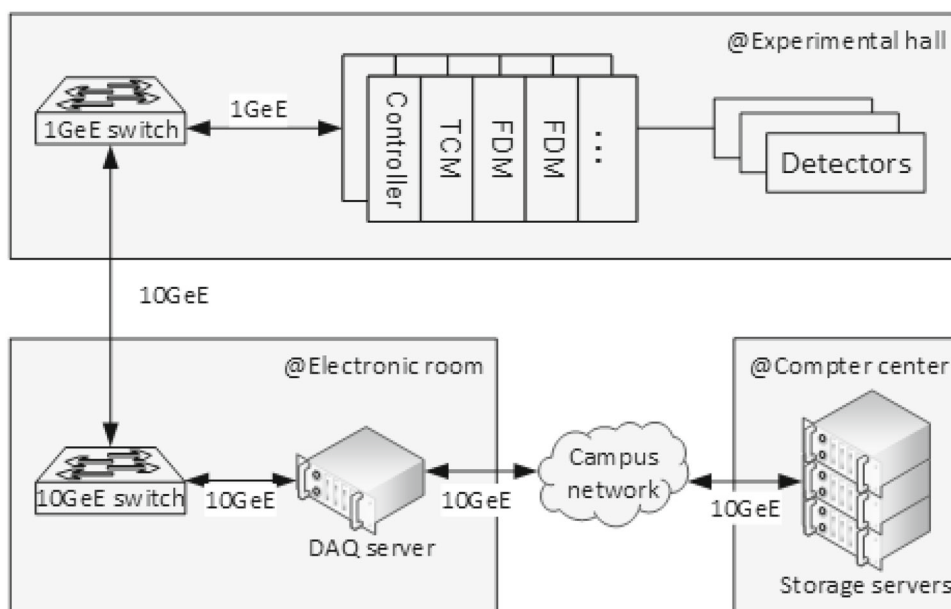
Fig. 32 Photography of electronics modules (from left to right: FDM, TCM, SCM and readout crate)

Common readout electronics

Good-performance electronics is a mandatory part of advanced spectrometers. Facing the challenge of high neutron flux, Back-n brings full digital trigger mechanism [69] and readout electronics [70,71] with high performance. Figure 30 shows the principle of signal readout and data acquisition. On the top side, signal from neutron detector is fed into the signal condition module to generate proper signals which is compatible with the ultra high-speed digitizer. With the help of folding structure of analog digital converter, full digitized waveform of detector signal is obtained with very good magnitude and time resolution. The sampling rate can reach up to 1 GSas, while the resolution can be 12 bit. Based on the digitized waveform data, full digital trigger algorithm is

proposed in Back-n as shown in Fig. 30. The L1 hardware digital algorithm is executed on FPGA (field programmable gate array). On each digitizer local FPGA, digitizing data stream is divided into two branches in parallel, one is fed into trigger match FIFO waiting for global trigger, and another one is fed into the sub-trigger processing module simultaneously. In the L1 hardware trigger structure, there is one master global trigger module, which receives all sub-trigger packet from all local trigger modules on each digitizer to generate the global trigger signal based on specific algorithm to indicate the valid good event occurs. This global trigger signal should be fanned out to each trigger match FIFO so that digitizer can readout the correct data corresponding to this good event. After being built, good event data are finally transmitted to the data acquisition server through ethernet.

Fig. 33 Hardware structure of DAQ system



Besides the waveform measurement, in order to obtain the neutron energy precisely, the neutron TOF (time-of-flight) should be measured precisely in the electronics. The time-to-digital converter based on FPGA is adopted in readout electronics [72]. With experiment and evaluation, the accuracy of TOF can reach about 280 ps which is good for Back-n application.

To fulfill the full digital trigger algorithm efficiently, it is necessary to use industry advanced readout platform with the ability of excellent data transmitting throughput and system synchronization. Back-n adopts the PXIe platform to be the readout crate as shown in Fig. 31. The PXIe platform is based on high-speed serial PCIe bus, which can support ultra-high-speed of data bandwidth. Meanwhile, there are several differential buses with star structure on backplane (PXIE_DSTARA, PXIE_DSTARB and PXIE_DSTARC), which can support for the global clock and trigger distributing and sub-trigger packets gathering. There are three different modules in the PXIe crate including TCM (trigger & clock module), SCM (signal condition module) and FDM (field digitizer module) as shown in Fig. 32. The FDM effective number of bits can be better than 9.2 bit among the frequency range of 398MHz with sampling rate of 1GSas, which guarantees that the readout electronics can meet the requirements of all Back-n spectrometers, especially the BaF₂ spectrometer which has very fast signal edge.

DAQ

A data acquisition(DAQ) system is built for the general-purpose electronics and Back-n detectors. The hardware

structure of DAQ system is shown in Fig. 33. PXI chassis controllers connect to a DAQ server through 1GbE/10GbE network. Three storage servers are deployed at the remote computer center and Gluster File System(GlusterFS) with excellent performance [73] is chosen for the management of storage resources. The storage system is close to the offline computing node, so that offline users are able to access the raw data more efficiently. Waveform data digitized by FDM board are readout by PXI chassis controllers and transferred to the DAQ server. The DAQ data flow software assembles the waveform packages into T0 Fragments(A T0 Fragment contains all events generated by a neutron bunch). T0 Fragments are fast processed in parallel for quality monitoring purposes. The whole The DAQ data flow runs on a single DAQ server with 56 CPU cores, data are processed in pipeline from readout to storage.

The run control and monitoring software is developed based on Django web framework. It communicates with the data flow software through Redis [74], in-memory data structure store. Control messages are sent throw Redis Pub/Sub interface and status parameters are updated periodically in Redis by the data flow software. Most online processing results are ROOT objects, which are also serialized to JSON string and published in Redis like status parameters. The JavaScript ROOT(JSROOT) library allows reading and displaying ROOT objects in an efficient way, and its rendering is now very d by ROOT [75]. So, the JSROOT library is used for visualization of online processing results in the Back-n monitoring software. The implementation of control and monitoring GUI of Back-n is shown in Fig. 34

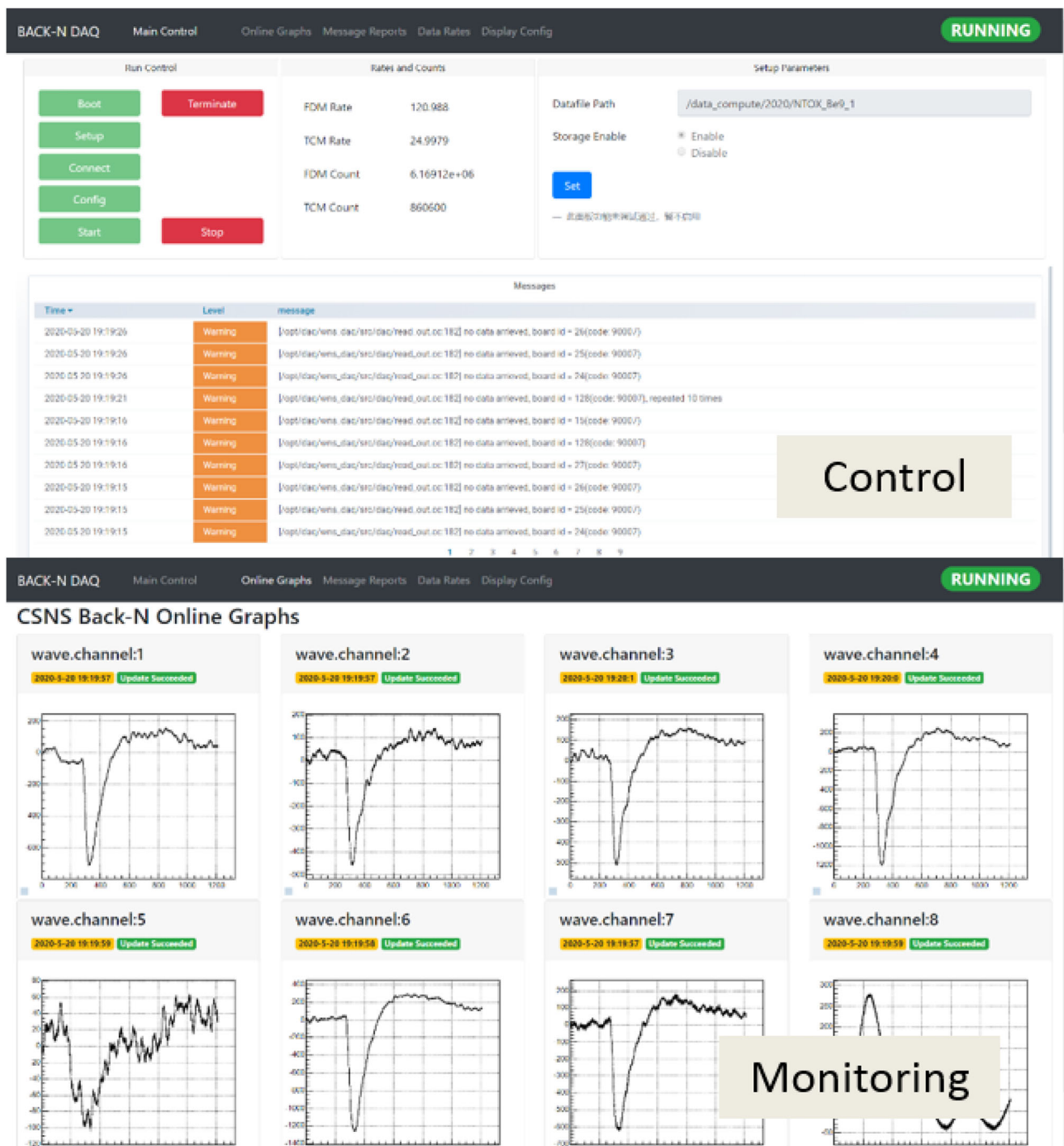


Fig. 34 GUI of run control and monitoring software

Summary

In past 5 years, a preliminary detector system has been established. In order to ensure the common operation of the day-one experiments, these detection systems such as the fission chamber and the C_6D_6 detectors adopt to the similar design of other white neutron beamlines. A update-

designed common electrics and DAQ also supported these system while the beamline running.

In future, some more difficult experiments were proposed. Such as the MTPC, the GTAF-II and the B-MCP were developed to meet these requirements. Most of these detectors are at the forefront of detector research. With the completion of these detectors in the next few years, it is believed that Back-n will achieve excellent physical results in the research of small

cross section and rare nuclear reaction physical events, the nucleosynthesis models of the astronomical nuclear physics and the archeology nondestructive detection, etc.

Acknowledgements The authors would like to acknowledge the funding support provided by the National Key R&D Program of China (Grant No. 2016YFA0401600).

Declarations

Conflict of interests We declare that we have no financial and personal relationships with other people or organizations that can inappropriately influence our work, there is no professional or other personal interest of any nature or kind in any product, service and/or company that could be construed as influencing the position presented in, or the review of, the manuscript entitled “Detector development at the Back-n white neutron source.”

Open Access This article is licensed under a Creative Commons Attribution 4.0 International License, which permits use, sharing, adaptation, distribution and reproduction in any medium or format, as long as you give appropriate credit to the original author(s) and the source, provide a link to the Creative Commons licence, and indicate if changes were made. The images or other third party material in this article are included in the article’s Creative Commons licence, unless indicated otherwise in a credit line to the material. If material is not included in the article’s Creative Commons licence and your intended use is not permitted by statutory regulation or exceeds the permitted use, you will need to obtain permission directly from the copyright holder. To view a copy of this licence, visit <http://creativecommons.org/licenses/by/4.0/>.

References

1. J. Wen, Y. Yang, Z. Wen et al., Measurement of the u-238/u-235 fission cross section ratio at csns back-n wns. *Ann. Nucl. Energy* **140**, 107301 (2020)
2. H. Bai, R. Fan, H. Jiang et al., Measurement of the differential cross sections and angle-integrated cross sections of the $6\text{Li}(n, t)4\text{He}$ reaction from 1.0 eV to 3.0 MeV at the csns back-n white neutron source. *Chin. Phys. C* **44**(1), 014003 (2020)
3. H. Jiang, W. Jiang, H. Bai, Z. Cui, G. Zhang, R. Fan, H. Yi, C. Ning, L. Zhou, J. Tang et al., Measurements of differential and angle-integrated cross sections for the $10\text{B}(n, \alpha)7\text{Li}$ reaction in the neutron energy range from 1.0 eV to 2.5 MeV. *Chin. Phys. C* **43**(12), 124002 (2019)
4. Exfor: Experimental nuclear reaction data. <https://www-nds.iaea.org/exfor/>. Accessed 14 Sep 2022
5. Z. Chen, A. Carlson, P. Finocchiaro, et al. Consultants meeting on neutron data standards (2020), <https://www-nds.iaea.org/index-meeting-crp/CM-NDS-2020-10/>. Accessed 14 Sep 2022
6. Q. Li, G. Luan, J. Bao et al., The 6LiF -silicon detector array developed for real-time neutron monitoring at white neutron beam at csns. *Nucl. Instrum. Methods Phys. Res., Sect. A* **946**, 162497 (2019)
7. mesytec GmbH & Co. KG. mesytec - detector readout systems (2022) <http://www.mesytec.com/>. Accessed 14 Sep 2022
8. H. CondC, *Nuclear Data Standards for Nuclear Measurements* (NUCLEARENERGYAGENCY, Uppsala, 1992)
9. A.D. Carlson, V.G. Pronyaev, D.L. Smith et al., International evaluation of neutron cross section standards. *Nuclear Data Sheets* **110**(12), 3215–3324 (2009)
10. D.A. Brown, M.B. Chadwick, R. Capote et al., Endf/b-viii0: The 8th major release of the nuclear reaction data library with cielo-project cross sections, new standards and thermal scattering data. *Nuclear Data Sheets* **148**, 1–142 (2018)
11. Y. Chen, G. Luan, J. Bao, et al. Neutron energy spectrum measurement of the back-n white neutron source at csns. *Eur. Phys. J. A*, **55**(7):1–10, 7 (2019). An erratum to this article is available online at <https://doi.org/10.1140/epja/i2019-12861-8>
12. Y. Giomataris, P. Rebourgeard, J.P. Robert, G. Charpak, MICROMEAS: a high-granularity position-sensitive gaseous detector for high particle-flux environments. *Nucl. Instrum. Methods Phys. Res. A* **376**(1), 29–35 (1996)
13. J. Pancin et al., Measurement of the n_{TOF} beam profile with a micromegas detector. *Nucl. Instrum. Methods Phys. Res. A* **524**(1), 102–114 (2004)
14. M. Diakaki et al., Development of a novel segmented mesh MicroMegas detector for neutron beam profiling. *Nucl. Instrum. Methods Phys. Res. A* **903**, 46–55 (2018)
15. B. Qi, Y. Li, D. Zhu, Z. Zhang, R. Fan, J. Pan, J. Feng, C. Liu, C. Feng, J. Liu, M. Shao, Y. Zhou, Y. Wang, H. Yi, Q. An, H. Bai, J. Bao, P. Cao, Q. Chen, Y. Chen, P. Cheng, Z. Cui, G. Minhao, F. Guo, C. Han, Z. Han, G. He, Y. He, Y. He, H. Huang, W. Huang, X. Huang, X. Ji, X. Ji, H. Jiang, W. Jiang, H. Jing, L. Kang, M. Kang, B. Li, L. Li, Q. Li, X. Li, Y. Li, R. Liu, S. Liu, X. Liu, G. Luan, Y. Ma, C. Ning, J. Ren, X. Ruan, Z. Song, H. Sun, X. Sun, Z. Sun, Z. Tan, H. Tang, J. Tang, P. Wang, Q. Wang, T. Wang, Z. Wang, Z. Wang, J. Wen, Z. Wen, W. Qingbiao, W. Xiaoguang, W. Xuan, L. Xie, Y. Yang, Yu. Li, Yu. Tao, Yu. Yongji, G. Zhang, J. Zhang, L. Zhang, L. Zhang, Q. Zhang, Q. Zhang, X. Zhang, Y. Zhang, Y. Zhao, L. Zhou, Z. Zhou, K. Zhu, P. Zhu, Measurement of the neutron beam profile of the back-n white neutron facility at csns with a micromegas detector. *Nucl. Instrum. Methods Phys. Res., Sect. A* **957**, 163407 (2020)
16. I.G. Irastorza et al., Gaseous time projection chambers for rare event detection: results from the T-REX project II Dark matter. *J. Cosmol. Astropart. Phys.* **2016**(01), 034 (2016)
17. I.G. Irastorza et al., Erratum: Gaseous time projection chambers for rare event detection: results from the T-REX project II Dark matter. *J. Cosmol. Astropart. Phys.* **2016**(05), E01 (2016)
18. F. Belloni, F. Gunsing, T. Papaevangelou, Micromegas for neutron detection and imaging. *Mod. Phys. Lett. A* **28**(13), 1340023 (2013)
19. J. Feng, Z. Zhang, J. Liu, B. Qi, A. Wang, M. Shao, Y. Zhou, A thermal bonding method for manufacturing micromegas detectors. *Nucl. Instrum. Methods Phys. Res., Sect. A* **989**, 164958 (2021)
20. C. Li et al., Design of the FPGA-based gigabit serial link for PandaX-III prototype TPC. *Radiat. Detect. Technol. Methods* **1**(2), 25 (2017)
21. C. Li, C.Q. Feng, D.Y. Zhu, S.B. Liu, Q. An, An optical fiber-based flexible readout system for micro-pattern gas detectors. *J. Instrum.* **13**(04), P04013–P04013 (2018)
22. D. Zhu, Z. Chen, H. Yi, K. Gao, C. Feng, R. Fan, K. Sun, W. Jiang, Q. Li, Y. Li, S. Liu, Csns back-n neutron time-of-flight measurement based on sca waveform-sampling readout electronics. *Atom. Energy Sci. Technol.* **54**(6), 1005–1012 (2020)
23. S.A. Wender, S. Balestrini, A. Brown, R.C. Haight, C.M. Laymon, T.M. Lee, P.W. Lisowski, W. McCorkle, R.O. Nelson, W. Parker, N.W. Hill, A fission ionization detector for neutron flux measurements at a spallation source. *Nucl. Instrum. Methods Phys. Res., Sect. A* **336**(1), 226–231 (1993)
24. M. Calviani, P. Cennini, D. Karadimos, V.V. Ketlerov, V.Yu. Kononov, W.I. Furman, A. Goverdowski, V. Vlachoudis, L. Zanini, A fast ionization chamber for fission cross-section measurements at

- n_tof. Nucl. Instrum. Methods Phys. Res. Sect. A **594**, 220–227 (2008)
25. Y. Yang, Z. Wen, Z. Han, M. Wang, R. Liu, J. Wen, X. Liu, Y. Chen, A multi-cell fission chamber for fission cross-section measurements at the back-n white neutron beam of csns. Nucl. Instrum. Methods Phys. Res., Sect. A **940**, 486–491 (2019)
 26. J. Wen, Y. Yang, Z. Wen, X. Liu, R. Liu, Z. Han, M. Wang, L. Zheng. A multi-layered fast ionization chamber prototype for fission cross section measurements. *J. Instrum.* (2018)
 27. J. Wen, Y. Yang, Z. Han, Z. Wen, R. Liu, Q. Chen, X. Liu, M. Wang, Accurate quantification of high-purity uranium in coatings by small solid angle method. *Appl. Radiat. Isot.* **164**, 109300 (2020)
 28. Z. Ren, Y. Yang, J. Wen et al., Measurement of the $^{236}\text{U}(n, f)$ cross section for neutron energies from 0.4 meV to 40 meV from the back-streaming white neutron beam at the china spallation neutron source. *Phys. Rev. C* **102**, 034604 (2020)
 29. Y. Maeda, H. Sakai, K. Fujita, M.B. Greenfield, K. Hatanaka, M. Hatano, J. Kamiya, T. Kawabata, H. Kuboki, H. Okamura et al., Differential cross section and analyzing power measurements for $n \rightarrow d$ elastic scattering at 248 meV. *Phys. Rev. C* **76**(1), 014004 (2007)
 30. P. Mermod, J. Blomgren, A. Hildebrand, C. Johansson, J. Klug, M. Österlund, S. Pomp, U. Tippawan, B. Bergenwall, L. Nilsson et al., Evidence of three-body force effects in neutron-deuteron scattering at 95 meV. *Phys. Rev. C* **72**(6), 061002 (2005)
 31. E. Ertan, T. Akdogan, M.B. Chtangeev, W.A. Franklin, P.A.M. Gram, M.A. Kovash, J.L. Matthews, M. Yuly, Cross sections for neutron-deuteron elastic scattering in the energy range 135–250 meV. *Phys. Rev. C* **87**(3), 034003 (2013)
 32. G. Zhang, Y.M. Gledenov, G. Khuukhenkhuu, M.V. Sedysheva, P.J. Szalanski, P. Edward Koehler, Y.N. Voronov, J. Liu, X. Liu, J. Han et al., $\text{Sm } 149(n, \alpha)\text{nd } 146$ cross sections in the meV region. *Phys. Rev. Lett.* **107**(25), 252502 (2011)
 33. Z. Wang, H. Bai, L. Zhang, H. Jiang, Y. Lu, J. Chen, G. Zhang, Y.M. Gledenov, M.V. Sedysheva, G. Khuukhenkhuu. Cross section measurement for the $\text{b } 10(n, t2\alpha)$ three-body reaction at 4.0, 4.5, and 5.0 meV. ii. experimental setup and results. *Phys. Rev. C*, **96**(4), 044621 (2017)
 34. R. Fan, H. Jiang, W. Jiang, G. Zhang, H. Yi, K. Sun, H. Bai, L. Zhou, C. Ning, Y. He et al., Detection of low-energy charged-particle using the δe -e telescope at the back-n white neutron source. Nucl. Instrum. Methods Phys. Res., Sect. A **981**, 164343 (2020)
 35. Y. Wang, Z. Sun, X. Wang, H. Yi, W. Jiang, R. Fan, L. Zhou, Y. He, C. Ning, Y. He, Y. Zhao, K. Sun, K. Gao, Characterization of low-pressure MWPC from $1\text{e}3$ to $1\text{e}5$ pa. *J. Instrum.* **16**(04), T04003 (2021)
 36. W. Jiang, H. Bai, H. Jiang, H. Yi, R. Fan, G. Zhang, J. Tang, Z. Sun, C. Ning, K. Sun et al., Application of a silicon detector array in (n, lcp) reaction cross-section measurements at the csns back-n white neutron source. Nucl. Instrum. Methods Phys. Res., Sect. A **973**, 164126 (2020)
 37. H. Jiang, W. Jiang, Z. Cui, G. Zhang, R. Fan, K. Sun, H. Bai, H. Yiwei, J. Liu, H. Yi et al., Measurement of the relative differential cross sections of the $^1\text{H}(n, \text{el})$ reaction in the neutron energy range from 6 meV to 52 meV. *Eur. Phys. J. A* **57**(1), 1–18 (2021)
 38. Z. Cui, H. Jiang, W. Jiang, G. Zhang, R. Fan, D. Pang, K. Sun, H. Bai, H. Yiwei, J. Liu et al., Measurement of relative differential cross sections of the neutron-deuteron elastic scattering for neutron energy from 13 to 52 meV. *Eur. Phys. J. A* **57**(11), 1–11 (2021)
 39. D. R. Nygren. Origin and development of the tpc idea. Nucl. Instr. Methods Phys. Res. Sect. A **907**, 22–30, (2018). *Advances in Instrumentation and Experimental Methods (Special Issue in Honour of Kai Siegbahn)*
 40. M. Heffner, D.M. Asner, R.G. Baker, J. Baker, S. Barrett, C. Brune, J. Bundgaard, E. Burgett, D. Carter, M. Cunningham, et al., A time projection chamber for high accuracy and precision fission cross-section measurements. Nucl. Instrum. Methods Phys. Res. Sect. A **759**, 50–64 (2014)
 41. M.S. Dixit, A. Rankin, Simulating the charge dispersion phenomena in micro pattern gas detectors with a resistive anode. Nucl. Instrum. Methods Phys. Res., Sect. A **566**(2), 281–285 (2006)
 42. Z. Chen, C. Feng, H. Chen, R. Fan, H. Yi, Z. Zhang, M. Gu, M. Zhang, W. Jia, J. Wang, Readout system for a prototype multi-purpose time projection chamber at csns back-n. *J. Instrum.* **17**, P05032 (2022)
 43. T. Slavicek, S. Petersson, S. Pospisil, G. Thungstrom, M. Slavickova, Sic based charged particle strip sensor spectrometer with neutron detection capability. *J. Instrum.* **15**(01), C01036 (2020)
 44. O. Obraztsova, L. Ottaviani, B. Geslot, G. de Izarra, O. Palais, A. Lyoussi, W. Vervisch, Comparison between silicon carbide and diamond for thermal neutron detection at room temperature. *IEEE Trans. Nucl. Sci.* **67**(5), 863–871 (2020)
 45. P. Vigneshwara Raja, J. Akhtar, C.V.S. Rao, S. Vala, M. Abhangi, N.V.L. Narasimha Murty, Spectroscopic performance studies of 4h-sic detectors for fusion alpha-particle diagnostics. Nucl. Instrum. Methods Phys. Res. Sect. A **869**, 118–127 (2017)
 46. N.R. Taylor, Y. Yu, M. Ji, P. Joshi, L.R. Cao, Direct metal contacts printing on 4h-sic for alpha detectors and inhomogeneous schottky barriers. Nucl. Instrum. Methods Phys. Res. Sect. A **989**, 164961 (2021)
 47. L.-Y. Liu, X. Ouyang, J.-L. Ruan, S. Bai, X.-P. Ouyang, Performance comparison between sic and si neutron detectors in deuterium-tritium fusion neutron irradiation. *IEEE Trans. Nucl. Sci.* **66**(4), 737–741 (2019)
 48. L. Wang, J. Jarrell, S. Xue, C. Tan, T. Blue, L.R. Cao, Fast neutron detection at near-core location of a research reactor with a sic detector. Nucl. Instrum. Methods Phys. Res. Sect. A **888**, 126–131 (2018)
 49. D. Szalkai, R. Ferone, F. Issa, A. Klix, M. Lazar, A. Lyoussi, L. Ottaviani, P. Tüttő, V. Vervisch, Fast neutron detection with 4h-sic based diode detector up to 500°C ambient temperature. *IEEE Trans. Nucl. Sci.* **63**(3), 1491–1498 (2016)
 50. Y. Shi, G. Bertuccio, Simulation of 4h-sic detectors for ultra fast particle spectroscopy. *J. Instrum.* **10**(03), P03013 (2015)
 51. C. Guerrero, U. Abbondanno, G. Aerts et al., The n_{tof} total absorption calorimeter for neutron capture measurements at cern. Nucl. Inst. Meth. A. **608**(3), 424–433 (2009)
 52. U. Abbondanno, G. Aerts, H. Alvarez et al., New experimental validation of the pulse height weighting technique for capture cross-section measurements. Nucl. Inst. Meth. A. **521**(2), 454–467 (2004)
 53. L.C. Mihailescu, L. Olah, C. Borcea et al., A new HPGe setup at gelina for measurement of gamma-ray production cross-sections from inelastic neutron scattering. Nucl. Inst. and Meth. A. **531**(3), 375–391 (2004)
 54. J. Ren, X. Ruan, J. Bao et al., The C_6D_6 detector system on the back-n beam line of csns. *Radiat. Detect. Technol. Methods* **3**, 52 (2019)
 55. Q. Wang, P. Cao, X. Qi et al., General-purpose readout electronics for white neutron source at china spallation neutron source. *Revi. Sci. Instrum.* **89**, 013511 (2019)
 56. J. Ren, X. Ruan, W. Jiang et al., Background study for (n, γ) cross section measurements with C_6D_6 detectors at csns back-n. Nucl. Instr. Meth. A **985**, 164703 (2021)
 57. B. Jiang, J. Han, W. Jiang et al., Monte-carlo calculations of the energy resolution function with geant4 for analyzing the neutron capture cross section of ^{232}Th measured at csns back-n. Nucl. Instr. Meth. A **1013**, 165677 (2021)
 58. X.X. Li, L.X. Liu, W. Jiang et al., New experimental measurement of $^{\text{nat}}\text{Er}(n, \gamma)$ cross sections between 1 and 100 eV. *Phys. Rev. C* **104**, 054302 (2021)

59. J. Ren, X. Ruan, W. Jiang et al., Neutron capture cross section of ^{169}Tm measured at the csns back-n facility in the energy region from 30 keV to 300 keV. *Chin. Phys. C* **46**, 044002 (2022)
60. Q. Zhang, G. He, G. Luan et al., Cross section measurement of neutron capture reaction based on hi-13 tandem accelerator. *Power Laser and Particle Beams* **33**(04), 0440 (2021)
61. Q. Zhang, G. Luan, G. He et al., Study of neutron shield and absorber for gamma total absorption facility. *Nucl. Phys. Rev.* **37**, 771 (2020)
62. Q. Zhang, G. Luan, M. Guo et al., Performance test of gamma-ray total absorption facility based on white neutron source. *Mod. Appl. Phys.* **12**(04), 040401 (2021)
63. Q. Zhang, G. Luan, J. Ren et al., Cross section measurement of neutron capture reaction based on back-streaming white neutron source at china spallation neutron source. *Acta Physica Sinica* **70**, 222801 (2021)
64. Z. Tan, J. Tang, H. Jing, R. Fan, Q. Li, C. Ning, J. Bao, X. Ruan, G. Luan, C. Feng, X. Zhang, Energy-resolved fast neutron resonance radiography at csns. *Nucl. Instrum. Methods Phys. Res., Sect. A* **889**, 122–128 (2018)
65. ELJEN TECHNOLOGY. Ej-426 - thermal neutron detector - eljen technology (2022). <https://eljentechnology.com/products/neutron-detectors/ej-426>
66. B. Jie, C. Yong-Hao, Z. Xian-Peng et al., Experimental result of back-streaming white neutron beam characterization at chinese spallation neutron source. *Acta Physica Sinica* **68**, 080101 (2019)
67. P. Von Der Hardt, H. Röttger (eds.), *Neutron Radiography Handbook* (Springer, Dordrecht Netherlands, 1981)
68. J.C. Overley, Element-sensitive computed tomography with fast neutrons. *Nucl. Instrum. Methods Phys. Res., Sect. B* **24–25**, 1058–1062 (1987)
69. L. Xie, P. Cao, T. Yu et al., Real-time digital trigger system for GTAF-II at CSNS back-n white neutron source. *J. Instrum.* **16**(10), P10029 (2021)
70. Q. Wang, P. Cao, X. Qi, T. Yu, X. Ji, L. Xie, Q. An, General-purpose readout electronics for white neutron source at china spallation neutron source. *Rev. Sci. Instrum.* **89**(1), 013511 (2018)
71. L. Xie, P. Cao, T. Yu et al., Prototype of readout electronics for GAEA gamma spectrometer of back-n facility at CSNS. *J. Instrum.* **17**(03), P03022 (2022)
72. T. Yu, P. Cao, X.Y. Ji et al., Electronics of time-of-flight measurement for back-n at csns. *IEEE Trans. Nucl. Sci.* **66**(7), 1095–1099 (2019)
73. G. Donvito, G. Marzulli, D. Diacono, Testing of several distributed file-systems (hdfs, ceph and glusterfs) for supporting the hep experiments analysis. *J. Phys. Conf. Ser.* **513**, 042014 (2014)
74. A.N. Gade, T.S. Larsen, S.B. Nissen, R.L. Jensen, Redis: A value-based decision support tool for renovation of building portfolios. *Build. Environ.* **142**, 107–118 (2018)
75. B. Bellenot, S. Linev, Javascript root. *J. Phys. Conf. Ser.* **664**, 062033 (2015)